



Crystal-facet-dependent activity and N₂ yield of Ag/CeO₂ catalysts for catalytic oxidation of N, N-Dimethylformamide

Xiaohan Guo, Chenxiao Dong, Meixingzi Gao, Dongsheng Ye, Qiguang Dai*, Wangcheng Zhan, Zhiqiang Wang, Li Wang, Aiyong Wang*, Yun Guo, Yanglong Guo

State Key Laboratory of Green Chemical Engineering and Industrial Catalysis, Research Institute of Industrial Catalysis, School of Chemistry and Molecular Engineering, East China University of Science and Technology, Shanghai 200237, PR China



ARTICLE INFO

Keywords:
Catalytic oxidation
NVOCS
DMF
Ceria morphology
N₂ yield

ABSTRACT

Shape-controlled CeO₂ with different exposed crystal facets, CeO₂ nanorods (110) and (100), nanocubes (100) and nano-octahedrons (111), were prepared as supports of Ag and then the catalytic oxidation of N, N-dimethylformamide (DMF) was investigated. Ag/CeO₂ nanorod (Ag/r-Ce) catalyst exhibits better dispersion of Ag species due to the abundant oxygen vacancies of CeO₂ (110) with outstanding anchoring effect, meanwhile, more Ag-O-Ce interfaces and Ag⁺ species are achieved because of the strong metal-support interaction and easy migration of oxygen species between Ag and CeO₂ (110). Ag/r-Ce catalyst exhibits excellent catalytic activity (T₉₀ = 158 °C), 100% yield of CO₂ at 240 °C, 80% yield of N₂ in the temperature range of 237–400 °C, unexceptionable H₂O-resistance, high stability at 240 °C for 120 h. In situ DRIFTS reveals that the dissociation of (O) C-N bond is firstly involved in DMF oxidation, and then the stepwise and repeated dehydrogenation of -N(CH₃)₂ and the insertion reaction of surface lattice oxygen occurs. Meanwhile the formed -HCO is completely oxidized into CO₂ and H₂O by surface adsorbed oxygen species and the two adjacent -NH₂ species combines into N₂.

1. Introduction

Volatile organic compounds (VOCs) have attracted extensive attention in recent years [1,2]. Nitrogen-containing volatile organic compounds (NVOCs), as one of VOCs, are much more harmful to the environment and human health than conventional VOCs, due to the serious injury to human organs and nervous system besides the contribution to the generation of global warming and photochemical smog. However, NVOCs such as N, N-dimethylformamide (DMF) is largely used as a versatile solvent and raw material in many industrial processes and released into the atmosphere. Variety of methods are employed in elimination of these pollutions, in which catalytic oxidation or combustion is the most promising method because of its low cost and high efficiency, but the generation of hazardous NO_x and even N₂O is troublesome and different from conventional VOCs [3]. Therefore, the screening of catalysts with both satisfying activity and yield of N₂ is a crucial issue.

Ag-based catalysts have been extensively applied in the selective catalytic oxidation of NH₃ (NH₃-SCO) [4,5], and selective catalytic reduction with NH₃ or CH_x (NH₃-SCR or CH_x-SCR) of NO [6,7], which

showed an outstanding activity and satisfying N₂ yield in relatively wide temperature range. Besides, Ag-based catalysts, especially Ag/CeO₂, also were widely applied in catalytic combustion of soot [8–10], HCHO [11,12] and other VOCs [13], and presented different catalytic performance. Generally, the tailoring of physicochemical properties of Ag species like the valence and size of Ag was crucial for the promotion of catalytic performance, which depended on the structure, acidity-basicity and the redox properties of supports. Wang et al. [4] indicated that the particle sizes of Al₂O₃ supports regulated the mean particle sizes and chemical states of Ag species and further influenced NH₃-SCO reaction. Better dispersed metallic Ag particles were obtained on nano-Al₂O₃, which resulted in better activity than Ag/mirco-Al₂O₃ catalyst. Nanba et al. [14] investigated the correlation of Ag species with the acidity-basicity properties of supports, and suggested that Ag species mainly existed as highly dispersed oxidized Ag species on acidic supports, such as ZSM-5 and Al₂O₃, while the presence of metallic Ag was observed on basic supports, such as ZrO₂ and MgO. Aneggi et al. [15] studied the properties of Ag species on CeO₂ with excellent redox property, and found that highly dispersed and stabilized Ag species in the form of positively charged Ag⁺ could be obtained because of the

* Corresponding authors.

E-mail addresses: daiqg@ecust.edu.cn (Q. Dai), wangaiyong@ecust.edu.cn (A. Wang), yguo@ecust.edu.cn (Y. Guo).

oxygen storage capacity of ceria. However, metallic Ag particles preferentially formed on Al_2O_3 and ZrO_2 . Grabchenko et al. [9] indicated the charge effect between Ag^+ and Ce^{3+} benefited the formation of $\text{Ag}-\text{CeO}_2$ interface. Ceria is extensively applied in the catalytic oxidation of VOCs as a catalyst or support owing to its abundant defects, outstanding redox ability and high oxygen storage capacity [12,16], more importantly, the exposed crystal facet was considered to be crucial in the catalytic performance for ceria-based catalysts due to different surface properties such as the atom arrangement, the formation energy of oxygen vacancy (2.69, 2.97 and 3.30 eV for (110), (100) and (111) facets [17]) and the adsorption ability of reactants. Dai et al. [18] found that CeO_2 nanorod with the exposed (110) and (100) planes exhibited remarkable performance for catalytic combustion of 1, 2-dichloroethane, since CeO_2 nanorod possessed larger concentration of oxygen vacancies, smaller crystal size and higher migration ability of oxygen. Li et al. [19] found that both the activity and stability were structure-sensitive for ceria in Deacon reaction, CeO_2 nanorod was the best candidate and depended on its exposed facets and complete oxygen storage capacity (OSC_c). Huang et al. [20] revealed that Ru/ CeO_2 using CeO_2 nanorods as the support presented more Ru^{4+} species and Ru-O-Ce interface and was beneficial to catalytic combustion of chlorobenzene, which signified that the exposed facet of CeO_2 resulted in the differences in status and structure of the supported metals. Wang et al. [21] revealed that Ru/ CeO_2 nanorods possessed higher activity than CeO_2 nanocubes and nano-octahedrons for catalytic oxidation of propane owing to the abundant surface oxygen vacancy around the interface of Ru-O-Ce. Sun et al. [22] disclosed that the Cu-O-Ce interface structures and the content of oxygen vacancy were determined by the exposed facet of ceria supports, moreover abundant $\text{Cu}^+-\text{O}_2-\text{Ce}^{3+}$ interfacial sites and oxygen vacancies benefited the promotion of NH_3 -SCO activity. Chang et al. [23] revealed that the interaction between Ag species and CeO_2 nanocubes (c- CeO_2) with mainly exposed (100) facets were more intensive than that between Ag species and CeO_2 nanorods (r- CeO_2) with exposed (110) and (100) crystal planes, which resulted in more oxidized Ag species on r- CeO_2 . Wang et al. [24] found that Ag species presented on CeO_2 nanocubes exposed (100) in form of metallic Ag^0 owing to the weak interaction between CeO_2 and Ag species which benefited the contact between soot and active species for the oxidation of soot.

However, the catalytic performance of Ag/ CeO_2 catalyst for the catalytic oxidation of NVOCs and the structure-activity relationship have not yet been investigated. In this work, 5 wt.% Ag was loaded on the shape-controlled ceria supports prepared by hydrothermal method, then the catalytic oxidation of N, N-dimethylformamide (DMF) as a representative of NVOCs was evaluated. Several characterizations such as TEM, EDS-Mapping, XRD, Raman, EPR, XPS, H₂-TPR, O₂-TPD, and in situ DRIFTS were performed to elucidate effects of the exposed crystal facets of CeO_2 support on Ag species and the structure-activity relationship of Ag/ CeO_2 catalyst, and the possible reaction mechanism of DMF oxidation was proposed.

2. Experimental

2.1. Preparation of shape-controlled CeO_2 supports

Three shape-controlled CeO_2 , namely CeO_2 nanorods (mainly exposed (100) and (110) crystal facets), nanocubes (mainly exposed (100) crystal facet) and nano-octahedron (mainly exposed (111) crystal facet), were prepared by hydrothermal method reported previously [25, 26], and the detailed description of preparation procedures was as follow.

2.1.1. Synthesis of CeO_2 nanorods

To obtain CeO_2 nanorods (r-Ce), in a typical synthesis, 10 mL $\text{Ce}(\text{NO}_3)_3$ (0.4 M) aqueous solution was dropped into 70 mL NaOH (6.8 M) solution under stirring. Then the mixture was placed into a Teflon-lined autoclave and kept at 100 °C under hydrothermal condition for 24 h.

The precipitates were centrifuged and washed 5 times until pH = 7, transferred into the oven at 60 °C for 12 h, and then calcined in a muffle furnace with a heating rate of 2 °C/min to 500 °C for 4 h.

2.1.2. Synthesis of CeO_2 nanocubes

The synthesis process of CeO_2 nanocubes (c-Ce) was similar to the process of CeO_2 nanorods mentioned above, except for the hydrothermal temperature was increased to 180 °C.

2.1.3. Synthesis of CeO_2 nano-octahedrons

The typical preparation of CeO_2 nano-octahedron (o-Ce) was as follows. Firstly, 70 mL Na_3PO_4 (7×10^{-5} M) aqueous solution was dropwise mixed into 10 mL $\text{Ce}(\text{NO}_3)_3$ (0.3 M) solution under stirring. Then, the mixed solution was placed into a Teflon-lined autoclave and kept at 200 °C under hydrothermal condition for 20 h. The precipitates were centrifuged and washed 5 times until pH = 7, transferred into the oven at 60 °C for 12 h, and then calcined in a muffle furnace with a heating rate of 2 °C/min to 500 °C for 4 h.

2.2. Preparation of Ag/ CeO_2 catalysts

AgNO_3 was used as the precursor to fabricate 5 wt.% Ag/ CeO_2 catalysts through conventional incipient wetness impregnation method. Suitable amount of AgNO_3 solution was added into the corresponding CeO_2 supports under stirring. After impregnation, the samples were kept statically at 25 °C for 6 h, then were placed into an oven at 80 °C for 12 h and calcined in a muffle furnace with the heating rate of 2 °C/min to 400 °C for 4 h. The obtained catalysts were denoted as Ag/r-Ce, Ag/c-Ce and Ag/o-Ce, respectively. Additionally, Ag/ CeO_2 (CeO_2 support was fabricated by decomposition of $\text{Ce}(\text{NO}_3)_3$ at 500 °C) catalysts with several Ag loadings were also fabricated and the catalytic performance for the catalytic oxidation of DMF was presented in Fig. S1.

2.3. Evaluation of catalytic performance

The catalytic performance including the activity and selectivity for the catalytic oxidation of DMF were carried out in a fixed-bed reactor at atmospheric pressure with stepwise heating program. Typically, 1500 ppm DMF was injected through a syringe pump and 100 mL/min desiccative air was applied as the reaction gas passing through 100 mg catalyst (40–60 mesh). When the effect of water was investigated, 5 vol. % H_2O was injected with two tandem bubblers in water bath (33 °C) and 95 mL/min dry air flow passed through the tandem bubblers. An on-line gas chromatography (GC 2060) with flame ionization detector (FID) and methane converter was applied to detect the organic compounds (DMF and byproducts), CO and CO_2 . Specifically, an SE-54 capillary column (30 m × 0.32 mm × 0.5 μm) was applied to detect DMF, DMA and other organic products, and an TDX-01 packed column passing through methane converter was used to detect CO and CO_2 . N-containing organic byproducts were qualitatively determined by PerkinElmer Clarus 680 GC/Clarus SQ 8 T MS system with an Elite-1MS capillary column (60 m × 0.25 mm × 1 μm). The concentrations of NO, NO_2 in the off-gas were detected by Thermo Scientific model 42i-L NO- NO_2 - NO_x analyzer, N_2O , NH_3 were detected by a gas cell equipped FT-IR spectrometer. The DMF conversion (assigned as X_{DMF}), CO_2 yield (assigned as Y_{CO_2}) and N_2 yield (assigned as Y_{N_2}) were calculated as follows:

$$X_{\text{DMF}} = \frac{[\text{DMF}]_{\text{in}} - [\text{DMF}]_{\text{out}}}{[\text{DMF}]_{\text{in}}} \times 100\%$$

$$Y_{\text{CO}_2} = \frac{[\text{CO}_2]_{\text{out}} - [\text{CO}_2]_{\text{in}}}{3 \times [\text{DMF}]_{\text{in}}} \times 100\%$$

$$Y_{\text{N}_2} = \frac{X_{\text{DMF}} \times [\text{DMF}]_{\text{in}} - [\text{NO}] - [\text{NO}_2] - [\text{NH}_3] - 2 \times [\text{N}_2\text{O}]}{[\text{DMF}]_{\text{in}}} \times 100\%$$

$[\text{DMF}]_{\text{in}}$ and $[\text{DMF}]_{\text{out}}$ were the inlet and outlet concentrations of

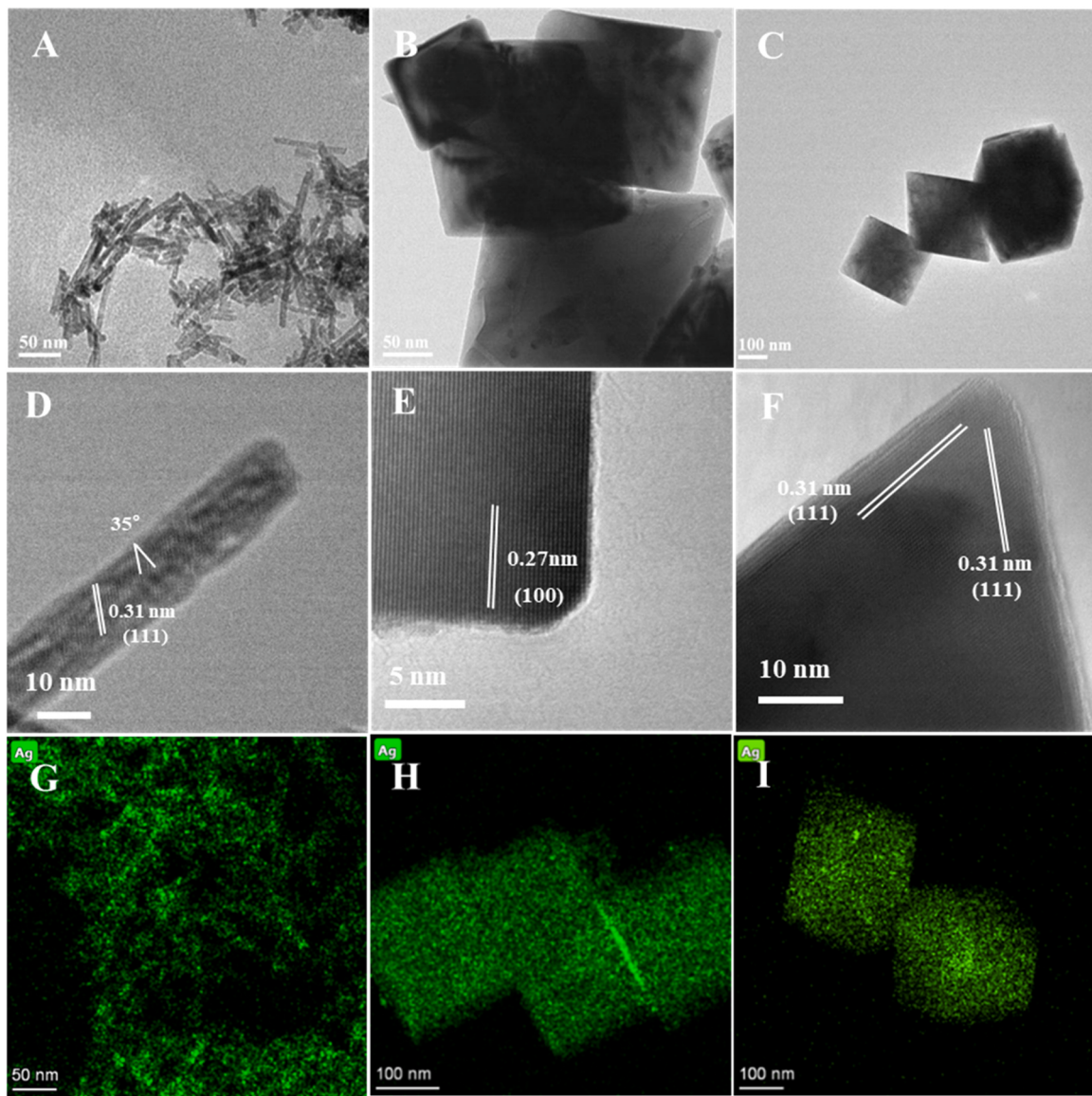


Fig. 1. TEM, HRTEM images and EDS Mapping of Ag/CeO₂ catalysts: Ag/r-Ce (panels A, D and G), Ag/c-Ce (B, E and H), Ag/o-Ce (C, F and I).

DMF. [CO₂]_{in} and [CO₂]_{out} were the inlet and outlet concentrations of CO₂. [NO], [NO₂], [NH₃] and [N₂O] were the concentrations of NO, NO₂, NH₃ and N₂O in the effluent.

2.4. Catalyst characterization

Transmission electron microscopy (TEM) images of CeO₂ supports were recorded on a JEM-2100 transmission electron microscope with the operating voltage at 200 kV. TEM images of Ag/CeO₂ catalysts were performed using ThermoFisher Talos F200X (FETEM, 200 kV). The energy dispersive X-ray spectroscopy (EDS) was conducted with 4 in-column Super-X detectors. Powder X-ray diffraction (XRD) patterns were performed by a Bruker D8 Focus diffractometer with Cu K α radiation (40 kV, 40 mA, $\lambda = 0.154056$ nm) and the scanning rate of 6°/min from 10° to 80° (the step size was set at 0.02°). Inductively coupled plasma atomic emission spectrometer (ICP-AES) was carried out on an Agilent 725 spectrometer. Raman spectra was performed by a Renishaw inVia reflex Raman spectrometer with Ar⁺ ion laser (325 nm) as the excitation source and the strength of the incident beam at 3 mW. The electron paramagnetic resonance (EPR) experiment was carried out on a Bruker EMX-8/2.7 electro-spin resonance spectrometer. X-ray

photoelectron spectroscopy (XPS) was carried out on a Thermo Scientific ESCALAB 250Xi spectrometer with Al K α excitation source ($h\nu = 1486.6$ eV). And the spectrum of samples was rectified by adventitious carbon (284.8 eV).

Temperature programmed reduction of hydrogen (H₂-TPR) experiments were carried out on a PX200 apparatus. 50 mg sample was placed at a U-shaped quartz tube and heated in 10% H₂/Ar mixing gas from 50 °C to 700 °C at the rate of 10 °C/min. The amount of H₂ consumption was measured by thermal conductivity detector (TCD) and the uptake value of H₂ was calculated and then calibrated by TPR profile of CuO to Cu. Temperature programmed desorption of oxygen (O₂-TPD) experiments were carried out on Micromeritics AutoChem II 2920 instrument coupled with a Hiden HPR20 mass spectrometer. 50 mg catalyst was placed at a U-shaped quartz tube and pretreated under 3 vol.% O₂/He atmosphere at 400 °C for 1 h. Then the sample was cooled to 50 °C and purged by He until the baseline of MS was stable. Afterwards, the O₂ desorption process was performed under He atmosphere from 50 to 700 °C with the rate of 10 °C/min.

In situ diffuse reflectance infrared fourier transform spectroscopy (In situ DRIFTS) was performed by a Nicolet Nexus 6700 FT-IR spectrometer with ZnSe material as the windows of in situ IR cell and MCT

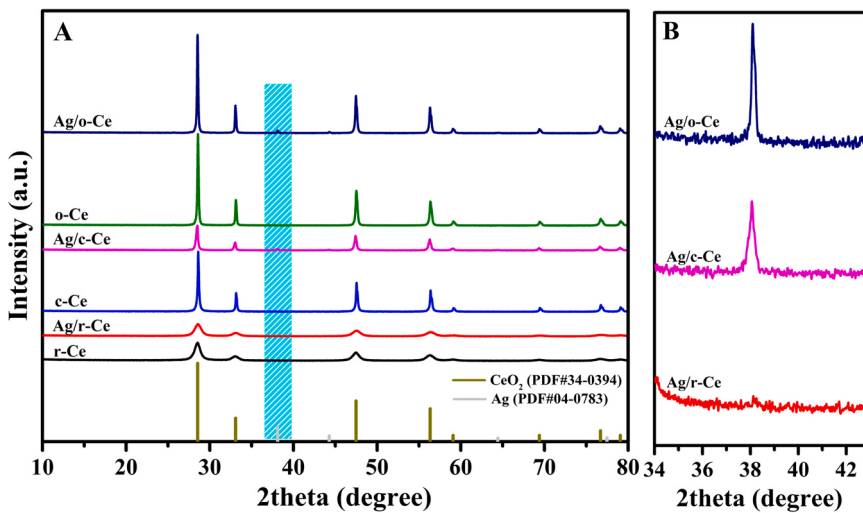


Fig. 2. XRD patterns of CeO_2 and Ag/CeO_2 catalysts (A), and enlarged patterns of Ag/CeO_2 catalysts (B).

detector. The catalyst was pretreated under 30 mL/min Ar or 10 vol.% O_2/Ar at 400 °C for 50 min before cooled to room temperature and the background spectrum was monitored during the cooling process. Then the saturated DMF gas was injected into the IR cell by Ar or 10 vol.% O_2/Ar and *in situ* DRIFTS spectra of adsorption species on the catalyst surface were collected with a stepwise increase in temperature.

3. Results and Discussion

3.1. Physicochemical properties of CeO_2 and Ag/CeO_2

3.1.1. Morphology, crystalline structure and texture properties

The morphology, exposed facets and spatial distribution of elements, investigated by TEM, HRTEM and EDS Mapping, were shown in Fig. 1, Figs. S2–S4. TEM images (Fig. S2A, B and C) indicated that the shape-controlled CeO_2 were successfully prepared, in practice, CeO_2 nanorods were disordered with about 10 nm in width and 50–100 nm in length, while CeO_2 nano-cubes and CeO_2 nano-octahedrons were non-uniform in size with the edge lengths about 70–100 nm and 150–200 nm, respectively. HRTEM images (Fig. S2D, E and F) further confirmed their morphologies and exposed crystal planes, basing on FFT patterns, the (111) crystal planes (the inter-plane d-spacing of 0.31 nm)

were observed on r-Ce, meanwhile, the orientation of these lattice fringes is rotated 35° relatively to the surface. According to the cubic geometry, the surfaces of r-Ce catalysts expose (110) and (100) facets [19]. c-Ce selectively exposed well-defined (100) facets (the inter-plane d-spacing of 0.27 nm) and o-Ce mainly exposed (111) facets (the inter-plane d-spacing of 0.31 nm) as reported previously [21]. Moreover, the morphologies, sizes and exposed crystal planes of CeO_2 supports were not affected after loading of Ag (Fig. 1A–F). The EDS mapping (Fig. 1G, H and I) revealed that Ag species was mostly finely dispersed on the surface of CeO_2 but depended on morphologies of CeO_2 (EDS-Mapping of Ce was shown in Fig. S3). For Ag/r-Ce catalyst, Ag species slightly aggregated and Ag nanoparticles grew to less than 5 nm, which was possibly ascribed to the preferential anchoring of Ag species on the oxygen vacancies of r-Ce exposing (100) and (110) facets with the minimum formation energy of oxygen vacancy. More uniform or random distribution of Ag species was observed on Ag/c-Ce and Ag/o-Ce catalysts due to the deficiency of oxygen vacancies. However, as shown in Fig. S4, large Ag nanoparticles were also detected on Ag/o-Ce catalyst, which resulted from the aggregation during the calcination process. To visualize the difference of Ag dispersion on Ag/r-Ce, Ag/c-Ce and Ag/o-Ce catalysts, HAADF images assisted with EDS-Mapping were performed to measure Ag particle sizes and the results were shown in

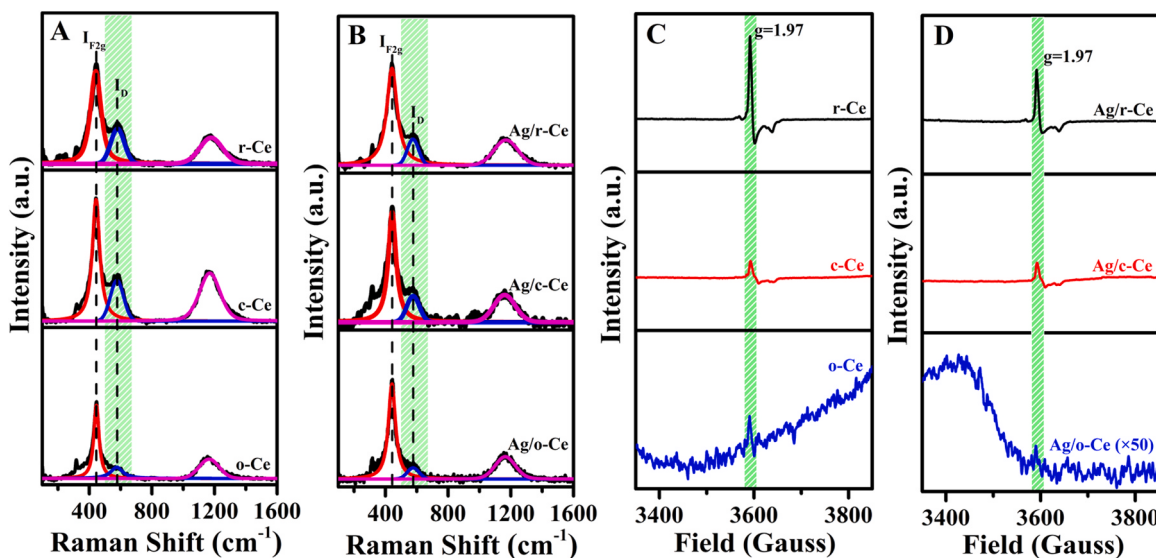


Fig. 3. Raman and EPR spectra of CeO_2 (A and C) and Ag/CeO_2 catalysts (B and D).

Table 1Texture, structure, surface and redox properties of CeO_2 and Ag/CeO_2 catalysts.

Catalysts	I_D/I_{F2g}^a	XPS			H_2 consumption ($\mu\text{mol/g}$) ^c	O_2 desorption (a.u.) ^d	T_{90} ($^{\circ}\text{C}$)
		$O_V/(O_V+O_L)$ (%) ^b	$\text{Ag}^+/(Ag^0+\text{Ag}^+)$ (%) ^b	$\text{Ce}^{3+}/(\text{Ce}^{3+}+\text{Ce}^{4+})$ (%) ^b			
Ag/r-Ce	0.27	25.2	49.0	0.23	862	18.77	158
Ag/c-Ce	0.24	23.2	29.3	0.20	87	4.07	223
Ag/o-Ce	0.12	20.6	0	0.18	40	1.88	296
r-Ce	0.38	26.0	-	0.26	485	3.21	240
c-Ce	0.33	23.8	-	0.23	64	1.20	285
o-Ce	0.15	21.7	-	0.19	43	1.00	328

^a Calculated from Raman results^b Calculated from O 1 s, Ag 3d and Ce 3d XPS data^c H_2 consumption below 600 $^{\circ}\text{C}$ calculated from H_2 -TPR data^d Normalized value of oxygen desorption of 200–600 $^{\circ}\text{C}$ from O_2 -TPD data

Fig. S5. The mean sizes of Ag particles were calculated to be 7.5, 26.2 and 43.4 nm for Ag/r-Ce, Ag/c-Ce and Ag/o-Ce catalysts, respectively. Due to the low content of oxygen vacancy on (111) facets and the weak interaction between Ag species and (111) facets, Ag species on o-Ce support was not stable and aggregated to be large nanoparticles.

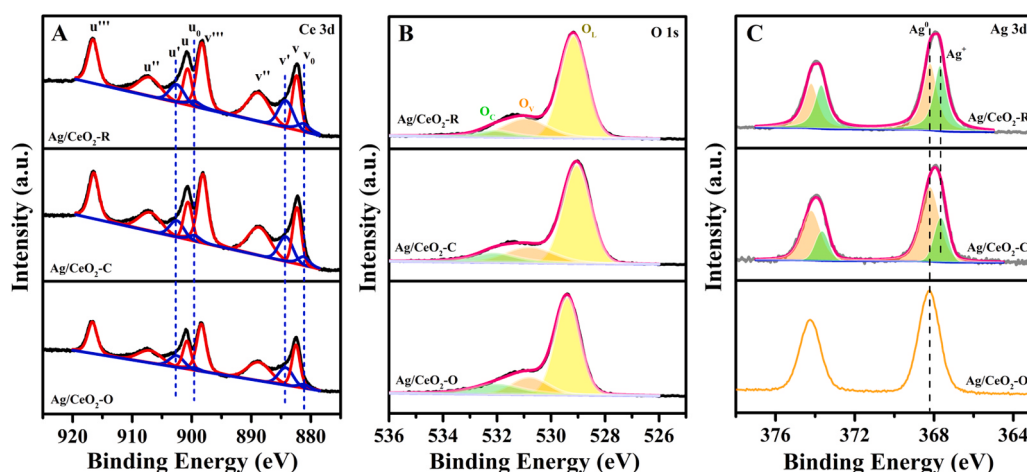
XRD patterns shown in **Fig. 2A** revealed that all CeO_2 samples only presented the characteristic peaks belonging to the fluoride CeO_2 , with seven major diffraction peaks at 28.6, 33.0, 47.5, 56.3, 59.2, 69.3 and 76.7 $^{\circ}$ (JCPDS card No. 34–0394), but the peak intensity of c-Ce and o-Ce was obviously higher than that of r-Ce, which was an indication of the higher crystallinity and bigger grain size. Based on Scherrer equation, their grain sizes were calculated to be 10.1, 49.8 and 54.5 nm for CeO_2 nanorod, nano-cube and nano-octahedron respectively, which was in agreement with the previous results since the grain size grew generally with the temperature of hydrothermal process [27]. After loading with 5 wt.% Ag, the visual change of the diffraction peaks including their 2 θ and intensities was not observed, however, the enlarged patterns (**Fig. 2B**) demonstrated that metallic Ag species locating at $2\theta = 38.1^{\circ}$ appeared on Ag/c-Ce and Ag/o-Ce catalysts, however, was unobtrusive on Ag/r-Ce [24], indicating that the higher dispersion of Ag species was obtained on r-Ce and coincided with EDS Mapping results.

Structure defects, such as oxygen vacancy, usually plays a decisive role in catalytic oxidation reactions, here, Raman and EPR spectra were performed. Raman spectra in the range of 200–1600 cm^{-1} were shown in **Fig. 3A** and three main peaks at 440–445, 575–580 and 1170–1175 cm^{-1} were observed on all samples. The former (strong peak) was corresponded to the F_{2g} mode of fluoride phase ceria, and the latter two (weak peaks) were assigned to the defect-induced (D) and second-order longitudinal modes. No obvious Raman shifts occurred after loading with Ag species, but the relative peak intensities decreased. In general, the ratio of I_D/I_{F2g} was calculated to roughly estimate the

content of intrinsic oxygen defects, as shown in **Table 1**, the I_D/I_{F2g} ratios were in the orders of r-Ce (0.38) > c-Ce (0.33) > o-Ce (0.15) and Ag/r-Ce (0.27) > Ag/c-Ce (0.24) > Ag/o-Ce (0.12). r-Ce based samples evidently presented a higher oxygen vacancy concentration, which was attributed to the low oxygen vacancy formation energy of r-Ce [19,28]. Additionally, the content of oxygen vacancy existing on Ag/CeO_2 obviously decreased in comparison to the pristine CeO_2 , which suggested that the Ag species preferentially anchored on the oxygen vacancies and corresponded with EDS mapping results. Then EPR was employed to further disclose some information of structure defects including oxygen vacancies, in general, the Ce^{3+} species adjacent to unpaired electrons (superoxide and peroxide species) was located at $g = 1.97$ and Ce^{3+} was highly relevant to appearance of oxygen vacancy [29,30]. **Fig. 3C** and **D** showed that r-Ce and c-Ce both displayed a sharp peak at $g = 1.97$ but the intensity of the latter was significantly weaker, while the EPR signal of o-Ce was almost silent even enlarged by 50 times, which demonstrated that the oxygen vacancies of r-Ce was the most abundant and consistent with the sequence obtained from Raman. Likewise, the introduction of Ag species only decreased the content of oxygen vacancy of ceria supports and other effects was not observed. Besides, the actual contents of Ag species for Ag/r-Ce, Ag/c-Ce and Ag/o-Ce catalysts measured by ICP-AES were 4.9, 4.9 and 4.9 wt.%, respectively.

3.1.2. Surface and redox properties

The chemical state of the surficial elements was investigated by XPS and presented in **Fig. 4** and **Fig. S6**. The Ce 3d spectra were extracted into ten peaks corresponding to two series of spin-orbit lines u and v ($\text{Ce}^{3d}_{3/2}$ and $\text{Ce}^{3d}_{5/2}$), six peaks marked as u, u'', u''' and v, v'', v''' were assigned to Ce^{4+} and the residual four peaks labeled as u_0 , u' and v_0 , v' were attributed to Ce^{3+} . The ratio of $\text{Ce}^{3+}/(\text{Ce}^{3+} + \text{Ce}^{4+})$ shown in

**Fig. 4.** Ce 3d (A), O 1s (B) and Ag 3d (C) XPS spectra of Ag/r-Ce, Ag/c-Ce and Ag/o-Ce catalysts.

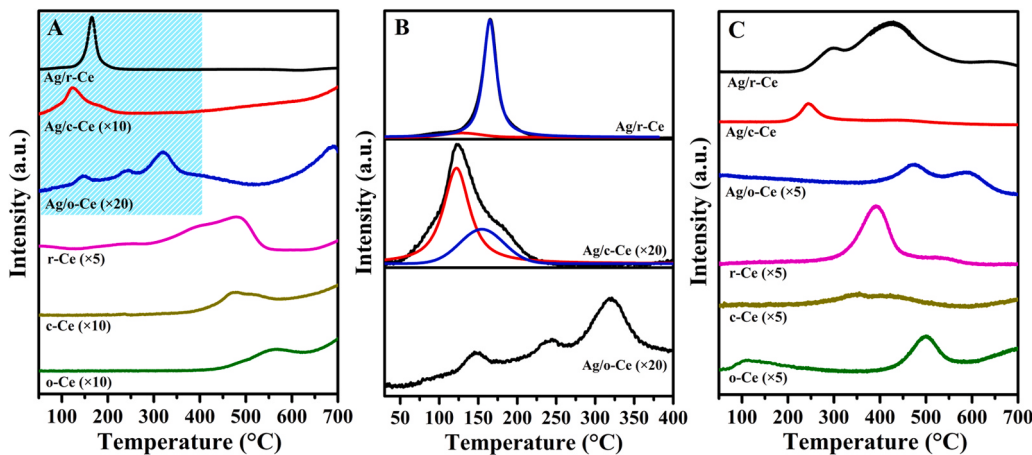


Fig. 5. H₂-TPR profiles of CeO₂ and Ag/CeO₂ catalysts (A), enlarged H₂-TPR profiles of Ag/CeO₂ catalysts in the range of 30–400 °C (B) and O₂-TPD (C) profiles of CeO₂ and Ag/CeO₂ catalysts.

Table 1 were calculated and in the following order: r-Ce (0.26) > c-Ce (0.23) > o-Ce (0.19) and Ag/r-Ce (0.23) > Ag/c-Ce (0.20) > Ag/o-Ce (0.18). Generally, the content of Ce³⁺ was highly associated with the concentration of surface oxygen vacancies and thus r-Ce, c-Ce and o-Ce sequentially reduced, and also confirmed Raman and EPR results. Moreover, the content of surface Ce³⁺ decreased expectedly after loading of Ag species due to the preferential anchoring of Ag species on the oxygen vacancies. As reported results [31,32], oxygen vacancies benefited the anchoring of noble metals and stabilized these adsorbed metals. And the charge interaction of Ag⁺ and Ce³⁺ in the interface also enhanced the interaction between Ag species and CeO₂ at the cost of partial Ce³⁺ species [9]. The binding energies of Ce 3d_{3/2} were located at 916.1, 916.0 and 916.4 eV, respectively, for r-Ce, c-Ce and o-Ce, while those were located at 916.7, 916.6 and 916.7 eV, respectively, for Ag/r-Ce, Ag/c-Ce and Ag/o-Ce catalysts. The increase of binding energy of Ce 3d_{3/2} after introduction of Ag species was 0.6, 0.6 and 0.3 eV, respectively, which demonstrated the interaction between Ag species and o-Ce support was weaker than those between Ag species and r-Ce and c-Ce supports. The O 1 s XPS spectra was extracted into three peaks and assigned to O_C at 532.0 eV (surface chemisorbed oxygen species, like OH⁻ and CO₃²⁻), O_V at 530.6 eV (chemisorbed oxygen species on oxygen vacancies of CeO₂) and O_L at 528.6 eV (CeO₂ lattice oxygen). The ratios of O_V / (O_V + O_L) were well calculated and summarized in **Table 1**, and decreased as the sequence of r-Ce (26.0%) > c-Ce (23.8%) > o-Ce (21.7%) and Ag/r-Ce (25.2%) > Ag/c-Ce (23.2%) > Ag/o-Ce (20.6%). The O_V amount of r-Ce based catalyst was more than those of other two catalysts, illustrating that the abundant structure defects could significantly enhance the concentration of chemically adsorbed oxygen. In general, O_V behaved better than lattice oxygen in oxidation reactions due to its stronger mobility, which was also considered to be instrumental in DMF oxidation.

The chemical state of Ag was also distinguished by Ag 3d XPS, and two symmetric Ag 3d_{5/2} peaks were observed and the splitting was 6 eV. The peak could be further divided into two peaks at 368.2 and 367.7 eV on Ag/c-Ce and Ag/r-Ce catalysts but failed on Ag/o-Ce catalyst (only one peak was located at 368.2 eV), which indicated that only metallic Ag species appeared on the latter catalyst, while the positively charged such as Ag⁺ or Ag₂O species and metallic Ag species co-existed on the former two catalysts. Furthermore, the relative content of metallic Ag species and positively charged Ag species was 70.7% and 29.3% on Ag/c-Ce catalyst while Ag/r-Ce catalyst presented more positively charged Ag species as much as 49.0% (**Table 1**), accordingly, the chemical state of Ag species closely associated with the exposed crystal plane of CeO₂ supports. Pure Ag₂O sample was known to decompose easily as the temperature reached 300 °C. However, the (110) and (100) facets

exposed r-Ce had high contents of oxygen vacancy and Ce³⁺ on its surface, thus enhancing the dispersion and metal-support interaction (MSI) between r-Ce and Ag species through charge interaction of Ce³⁺ and Ag⁺, which benefited presence of Ag⁺ species by the Ag-O-Ce interface. Less Ag⁺ species was detected on Ag/c-Ce because of lower content of Ce³⁺ and weaker MSI between Ag and c-Ce support. By contrast, the contents of oxygen vacancy and Ce³⁺ on (111) facets exposed o-Ce were insufficient, so MSI between Ag species and o-Ce was negligible, which made Ag species on o-Ce was not stable and aggregated to be large Ag nanoparticles during the calcination process.

The redox properties of oxygen species presenting in the pristine CeO₂ and Ag/CeO₂ catalysts, such as the reducibility and oxygen species types or mobility, were measured by H₂-TPR and O₂-TPD, and the results were exhibited in **Fig. 5**. H₂ reduction profiles for the three pristine CeO₂ supports were shown in **Fig. 5A**, and there were two reduction peaks at the range of 300–600 °C and above 700 °C, which were due to the reduction of surface adsorbed or lattice oxygen species and bulk lattice oxygen species in CeO₂. Specifically, the reduction peak of r-Ce with the maximum at 480 °C was more visible than c-Ce and o-Ce. The H₂ consumption listed in **Table 1** followed the sequence of r-Ce (485 μmol/g) > c-Ce (64 μmol/g) > o-Ce (43 μmol/g), which was in accord with the fact that these surface adsorbed oxygen species were generally adsorbed on oxygen vacancies and the amount of oxygen vacancy decreased sequentially (corresponding to Raman, EPR and XPS results). (110) and (100) facets exposed r-Ce had the minimum formation energy of oxygen vacancy, which was important to adsorption and activation of oxygen species. Thus r-Ce possessed more surface adsorbed oxygen species than other two catalysts. After loading with 5 wt% Ag, the low temperature reduction peaks obviously shifted to lower temperature, with the maximum from 480 °C to 166 °C of Ag/r-Ce, from 473 °C to 123 °C of Ag/c-Ce and from 563 °C to 146 °C, 240 °C and 320 °C of Ag/o-Ce (**Fig. 5B**), which demonstrated that the promotion effect of Ag species for active oxygen species of CeO₂ supports occurred, since presence of Ag species could weaken the Ce-O bond and improve the redox ability of surface oxygen species due to the reverse spillover effect of the oxygen species over CeO₂ supports through interface of Ag and CeO₂ [8,10]. Additionally, for Ag/r-Ce and Ag/c-Ce catalysts, the reduction peaks could be divided into two parts at 125 °C and 160 °C, attributing to the reduction of the active oxygen species on Ag surface by the reverse spillover effect and the active surface oxygen species of CeO₂ adjacent to Ag species which resulted from the effect of Ag species on weakening Ce-O bonds [8], respectively. Moreover, the H₂ consumption corresponding to Ag₂O at about 125 °C was 65 and 50 μmol/g for Ag/r-Ce and Ag/c-Ce, which was corresponding to the sequence of Ag⁺ content measured by Ag 3d XPS. The peaks at 146, 240 and 320 °C were assigned to the oxygen species of CeO₂ adjacent to Ag species and away from Ag

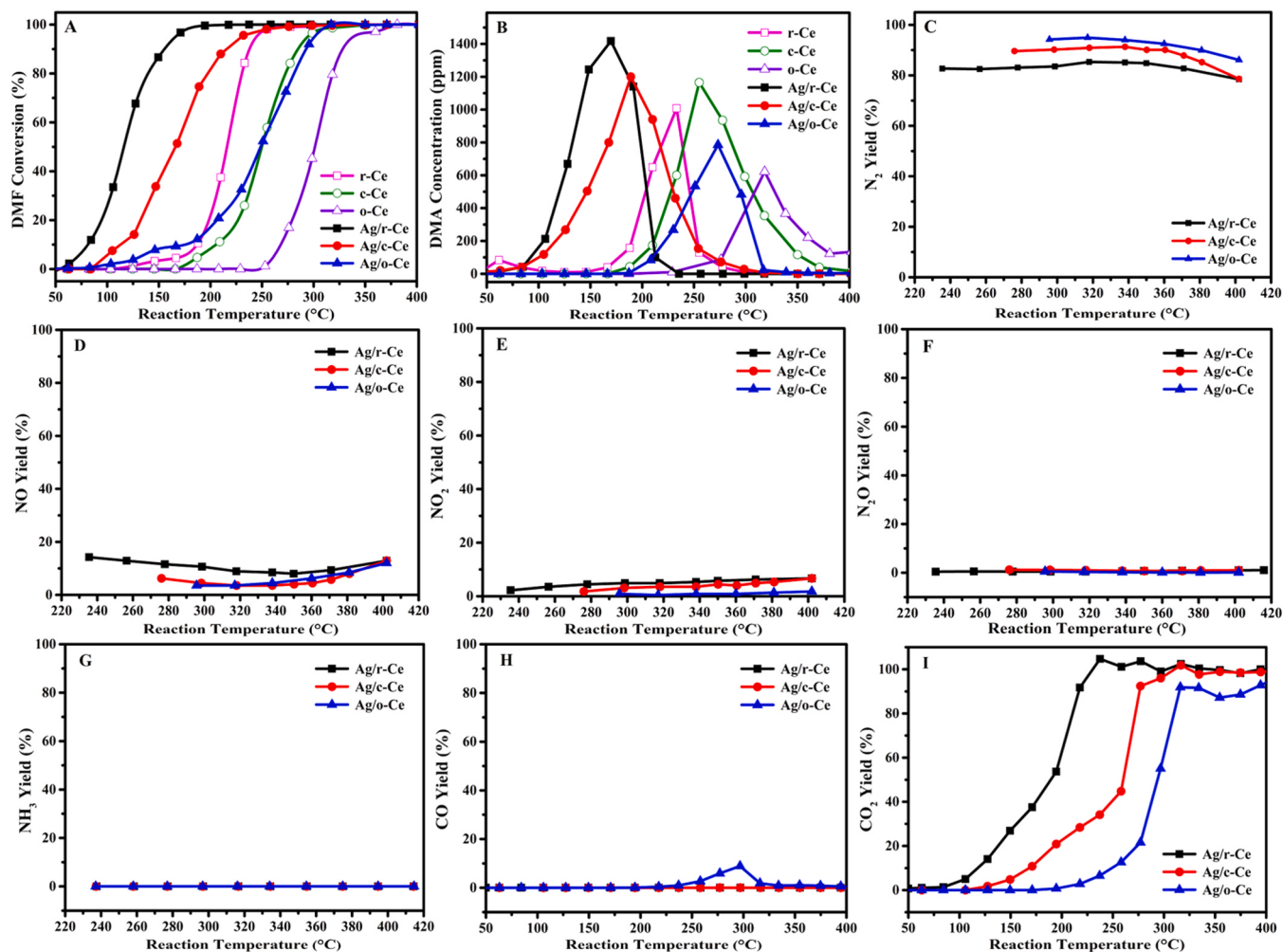


Fig. 6. Catalytic performance of CeO_2 and Ag/CeO_2 catalysts for catalytic oxidation of DMF (A), and the distribution of possible products: the concentration of DMA (B), the yield of N_2 (C), and the yields of NO (D), NO_2 (E), N_2O (F), NH_3 (G), CO (H) and CO_2 (I).

species for $\text{Ag}/\text{o-Ce}$. The lack of peak for Ag_2O species at 125°C was also in accord with the Ag 3d XPS result. Additionally, the H_2 consumption of total active oxygen species existing on Ag/CeO_2 was calculated and as follow: $\text{Ag}/\text{r-Ce}$ ($862 \mu\text{mol/g}$) $>>$ $\text{Ag}/\text{c-Ce}$ ($87 \mu\text{mol/g}$) $>$ $\text{Ag}/\text{o-Ce}$ ($40 \mu\text{mol/g}$), which showed the extremely excellent activity of oxygen species for $\text{Ag}/\text{r-Ce}$ catalyst. The splendid redox ability was thought to be highly related with the satisfying dispersion of Ag species over r-Ce and the strong interaction between Ag species and r-Ce support.

As shown in Fig. 5C, O_2 -TPD profiles indicated that only one main desorption peak was observed on the pristine CeO_2 in the range of $200\text{--}650^\circ\text{C}$, however, with different peak temperatures and intensity. In particular, the desorption peaks of r-Ce , c-Ce and o-Ce centered at 390°C , 352 and 430°C and 498°C were associated with the surface chemically adsorbed or surface lattice oxygen species, which was known as surface active oxygen species. Intrinsic oxygen vacancy benefits the mobility of bulk oxygen species to the surface, which reduces the desorption temperature and enhances the amount of surface oxygen species. The relative amount of these oxygen species was determined and summarized in Table 1 based on their peak intensity. r-Ce support presented the highest surface oxygen species while o-Ce support was the lowest, which was corresponding to the fact that r-Ce support behaved much more active than c-Ce and o-Ce supports. The desorption peaks shifted to lower temperatures after loading of Ag for the three shape-controlled supports, from 390°C to 300°C and 425°C , from 352°C and $425\text{--}245^\circ\text{C}$ and 430°C , and from 498°C to 473°C and 594°C for $\text{Ag}/\text{r-Ce}$, $\text{Ag}/\text{c-Ce}$ and $\text{Ag}/\text{o-Ce}$ catalysts. The peaks at $240\text{--}300^\circ\text{C}$ were

mainly associated with the surface oxygen species on Ag species and partial lattice oxygen of CeO_2 through the reverse spillover effect, and the peaks at $420\text{--}600^\circ\text{C}$ were associated with the surface and lattice oxygen species of CeO_2 neighboring Ag species or away from Ag species, which benefited the presence of oxygen species with higher activity, like O_2 and O^\bullet species. Notably, the interaction between Ag species and (100) or (110) facets was strong, thus promoting the reverse spillover effect of O species from CeO_2 to Ag species. Moreover, the highly dispersed Ag species and sufficient $\text{Ag}-\text{O}-\text{Ce}$ interfaces also contributed to more active oxygen species generated by Ag species (peaks at $420\text{--}600^\circ\text{C}$).

3.2. Catalytic oxidation of *N, N*-dimethylformamide

3.2.1. Activity, products distribution and stability

Fig. 6A showed the catalytic performance of pristine CeO_2 and Ag/CeO_2 catalysts for the catalytic oxidation of DMF. The r-Ce catalyst presented a significantly better activity and T_{90} of DMF oxidation (the temperature required to achieve 90% conversion) was 240°C , while up to 285°C and 328°C on c-Ce and o-Ce catalysts, due to the different adsorption and activation ability of oxygen. As shown in Fig. S7, the structures of (110), (100) and (111) facets of CeO_2 were built and the energies of oxygen adsorption on different facets were calculated to be 0.21 , 0.18 and 0.14 eV , respectively. Importantly, Ag species greatly promoted the intrinsic activity of ceria and T_{90} of $\text{Ag}/\text{r-Ce}$, $\text{Ag}/\text{c-Ce}$ and $\text{Ag}/\text{o-Ce}$ catalysts decreased to 158°C , 223°C , and 296°C , respectively. Additionally, it could be found that the reduction of T_{90} by 82°C was

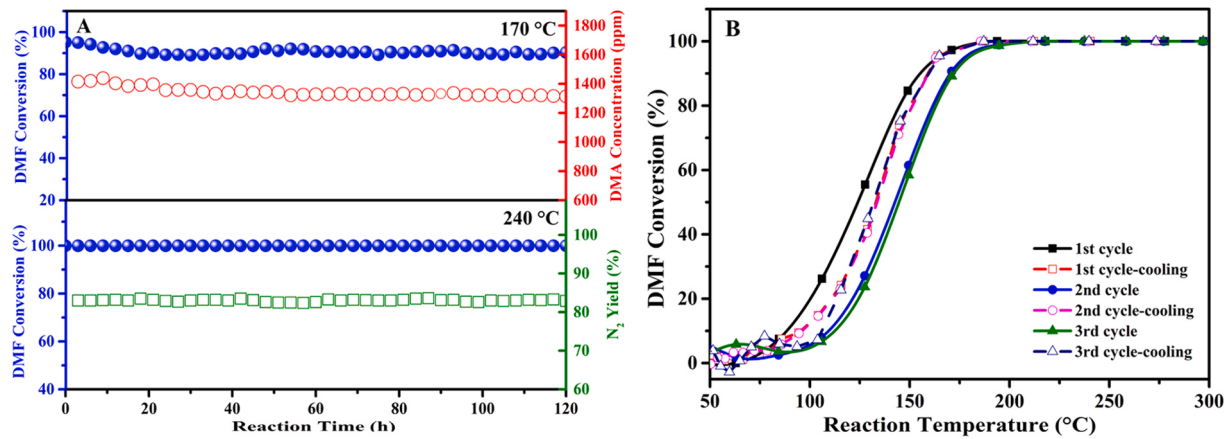


Fig. 7. Prolonged stability of Ag/r-Ce catalyst at 170 °C and 240 °C for catalytic oxidation of DMF (A) and cyclic stability of Ag/r-Ce catalyst during 3 times cycle testing (B).

achieved on r-Ce catalyst while those were only 62 °C and 32 °C on r-Ce and o-Ce catalysts respectively, which was related with the physical and chemical states of the loaded Ag species. The abundant oxygen vacancies on (110) and (100) facets provided high dispersion of Ag species and strong MSI between r-Ce and Ag species, and thus ensured delivery of

oxygen species, which made Ag/r-Ce catalyst the best in terms of the catalytic activity of DMF oxidation. In addition, various possible organic by-products such as dimethylamine (DMA), methylamine, tetramethylmethylenediamine and dimethylnitrosamine (shown in Fig. S8) and inorganic products such as NO, NO₂, N₂O, NH₃, CO, CO₂ and H₂O are

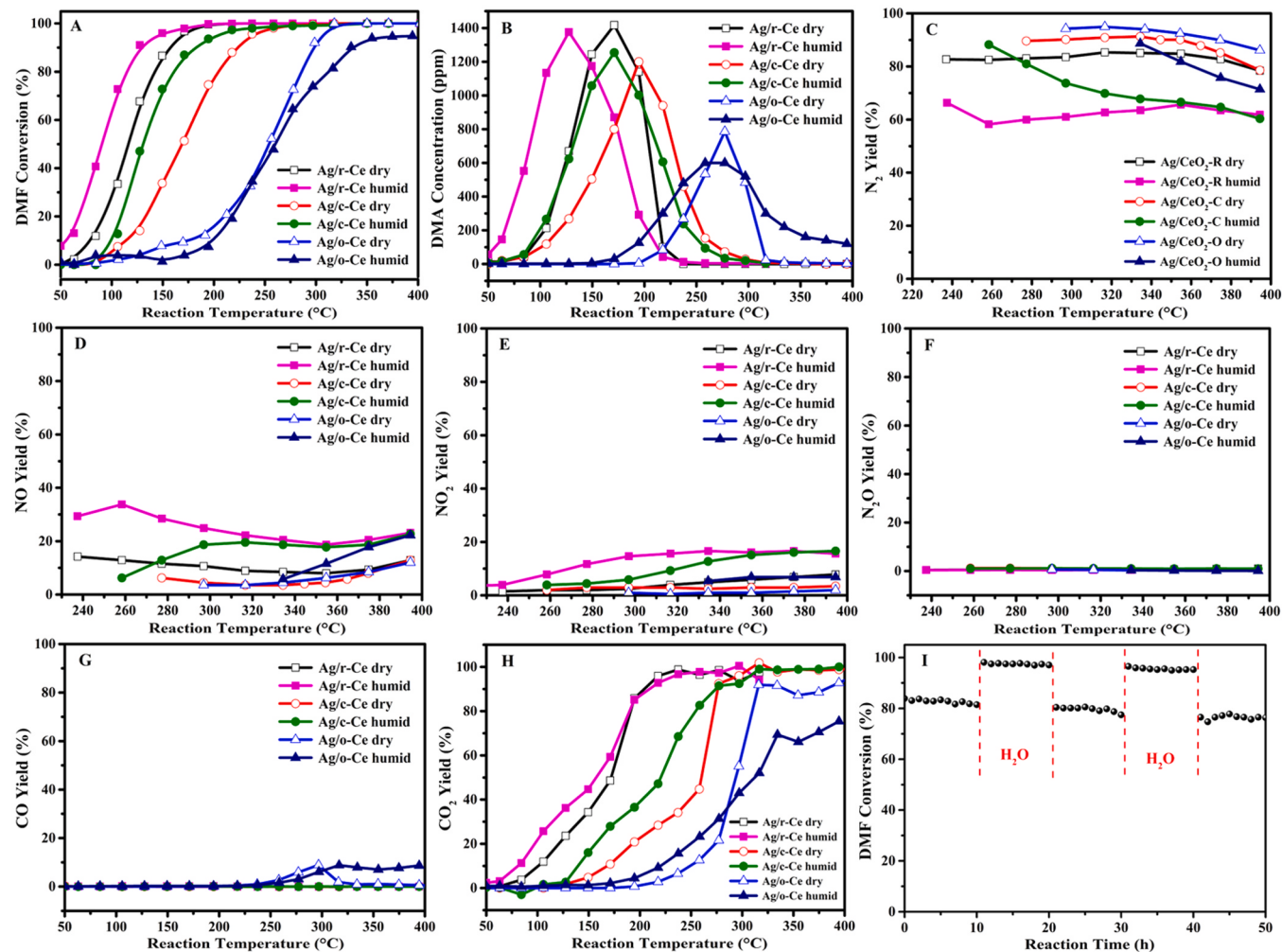


Fig. 8. Catalytic performance of Ag/CeO₂ catalysts for catalytic oxidation of DMF under humid condition (A), and the distribution of possible products under humid condition: the concentration of DMA (B), the yield of N₂ (C), and the yields of NO (D), NO₂ (E), N₂O (F), CO (G) and CO₂ (H). Effect of water on DMF conversion over Ag/r-Ce catalyst (I).

generally produced and must be concerned for a promising catalyst for the catalytic oxidation of DMF. Fig. 6B provided the temperature-concentration curves of the most abundant and stable DMA as one of the representative organic by-products. The maximum of 700–1200 ppm was detected over the pristine CeO_2 , the corresponding peak temperature and complete oxidation temperature increased orderly by r-Ce, c-Ce and o-Ce catalysts. The loading of Ag not only promoted the formation of DMA (with the maximum of about 800–1400 ppm) obviously, but also reduced the complete oxidation temperature, for example, Ag/r-Ce catalyst achieved the complete oxidation of DMA at 237 °C and followed by Ag/c-Ce (277 °C) and Ag/o-Ce (335 °C). These results suggested that the elimination of DMA heavily depended on the chemical-physical state of Ag species and redox ability of catalysts.

N_2 yield, as an important index of the catalytic oxidation for NVOCs, was shown in Fig. 6C. Ag/o-Ce catalyst displayed the best N_2 yield with a maximum of 95%, while Ag/r-Ce catalyst displayed the worst N_2 yield of only about 80%, which might be highly related with the redox ability of catalysts. Furthermore, N_2 yield of all Ag/CeO_2 catalysts increased slightly with increasing the reaction temperature and then decreased due to the combined effects of the selective catalytic reduction (SCR) of NO and the excessive oxidation of DMF. The high reaction temperature was detrimental since the promotion of the activity of surface oxygen species made the combination of N with O instead of another N. Sequentially, other main inorganic products such as NO, NO_2 , N_2O , NH_3 , CO and CO_2 were monitored on Ag/CeO_2 catalysts and displayed in Fig. 6D–I. As the major N-containing inorganic byproduct, NO yield was in the range of 3–15%. NO generation first decreased then increased with increasing the reaction temperature. Ag/o-Ce catalyst presented the least amount of NO yield and was corresponding to the curve of N_2 yield mentioned above, because the generation of NO was positively related with the redox properties of catalysts. The generation of NO was related with the direct combination of the dissociated N species and active oxygen species instead of adjacent N species. Besides, NO could also participate in the formation of N_2 through the SCR reaction with organic compounds in a suitable temperature range. The yield of NO_2 was stable and few on Ag/o-Ce catalyst (below 2%). However, the yield of NO_2 over Ag/r-Ce and Ag/c-Ce catalysts seemed to be positively related with the reaction temperature and reached 7% at 400 °C. N_2O and NH_3 were monitored by gas cell equipped IR, the yield of N_2O was stable (below 1%) while the generation of NH_3 was not observed, which was almost independence of catalysts and reaction temperature. CO and CO_2 , as the indication of the complete-oxidation degree, were presented in Fig. 6H, I and S9. A large yield of CO was detected over the pristine CeO_2 catalyst, and the maximum of 9% (r-Ce catalyst) to 13% (c-Ce and o-Ce catalysts) at about 325 °C was observed, and the generation of CO on r-Ce catalyst rapidly decreased at the higher reaction temperature. The presence of Ag tremendously inhibited formation of CO and even was undetectable on Ag/r-Ce and Ag/c-Ce catalysts, even though Ag/o-Ce catalyst only reached the maximum of 10%. Furthermore, CO_2 yield curves (Fig. 6I) also confirmed CO results, Ag/r-Ce and Ag/c-Ce catalysts showed 100% CO_2 yield while only 90% on Ag/o-Ce catalyst. Therefore Ag/r-Ce catalyst was a promising candidate for the catalytic oxidation of NVOCs due to the highest catalytic activity and 100% yield of CO_2 .

Furthermore, the prolonged and cyclic stability of Ag/r-Ce catalyst for the catalytic oxidation of DMF was evaluated at constant temperatures, such as 170 °C (T_{95}) and 240 °C (T_{100}), via three times cycle testing. As shown in Fig. 7A, the prolonged stability tests indicated that the conversion of DMF kept 100% stably for at least 120 h at 240 °C and stable DMF conversion even at 170 °C (a slight decline within the initial 20 h). The prolonged stability of DMA at 170 °C and N_2 yield at 240 °C were shown in Fig. 7A. The concentration of DMA increased slightly in the initial 10 h and the accumulation of DMA might be the reason for the slight decrease of DMF conversion. Besides, N_2 yield kept 83% stably during the prolonged test of Ag/r-Ce catalyst. Additionally, during three times cyclic stability testing shown in Fig. 7B, it could be found that the

catalytic activity of Ag/r-Ce catalyst decreased significantly after the first testing, however, kept stable in the following cycles and the further deactivation was not observed. Unexpectedly, the cooling-activity always stayed the same during the three tests, but fell in between the first heating-activity and the latter two heating-activity. The decrease of DMF conversion after the first testing might be related with accumulation of DMA on the highly active sites, which was also consistent with the slight increase of DMA concentration in the initial 10 h.

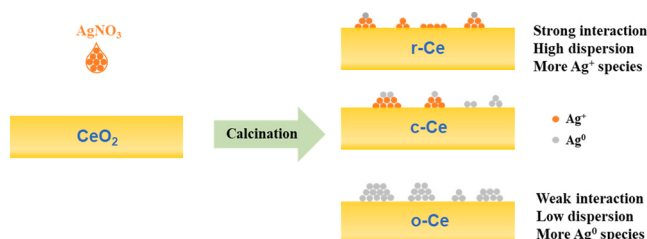
3.2.2. Effect of water on activity, stability and selectivity

To further evaluate the catalytic performance of shape-controlled Ag/CeO_2 catalysts under the real reaction conditions, 5 vol.% H_2O was injected into the feed gas. Fig. 8A revealed that the introduction of H_2O substantially promoted the catalytic oxidation of DMF on Ag/r-Ce and Ag/c-Ce catalysts especially in the low temperature range, T_{90} decreased by 30 °C and 40 °C compared with those of the dry condition, respectively. However, the promotion of H_2O was not observed on Ag/o-Ce catalyst and was even detrimental especially at higher temperature due to the competition between H_2O and O_2 over Ag/o-Ce catalyst which exhibited poor intrinsic redox ability. Additionally, effects of H_2O on DMA byproduct, N_2 and CO_2 yield were specially focused. As shown in Fig. 8B, the introduction of water hardly affected the maximum concentration of DMA except for the shift of temperature to lower ranges due to the increase of DMF conversion. Besides, the complete oxidation temperature of DMA stayed invariable for Ag/r-Ce and Ag/c-Ce catalysts which also demonstrated the little impact of water on the complete oxidation of DMA. However, water seemed to play crucial role in N_2 yield. All three morphology-controlled Ag/CeO_2 catalysts exhibited lower N_2 yield in humid condition compared with dry condition, which mainly resulted from the increase of NO and NO_2 yield (shown in Fig. 8D and E). Additionally, the yield of N_2O kept stable and below 1% (shown in Fig. 8F), and the generation of NH_3 was still not observed (not shown). Moreover, the yield of CO_2 exhibited high relationship with the conversion of DMF and the generation of CO were not detected for Ag/r-Ce and Ag/c-Ce catalysts. However, large amount of CO (with the maximum yield of 10%) was detected over Ag/o-Ce catalyst, especially in the humid condition, due to the competition of H_2O with O_2 mentioned above which made the active oxygen species insufficient. In order to further confirm the promotion of H_2O , the prolonged stability of Ag/r-Ce catalyst at 150 °C was investigated under the reaction conditions with and without 5 vol.% H_2O (Fig. 8I), as expected, the conversion of DMF increased from 83% to 96% after introduction of 5 vol.% H_2O and was stable within 50 h reaction.

3.3. Structure-activity relationship and reaction mechanism

3.3.1. Roles of physical-chemical states of Ag species and oxygen species

Ag-based catalysts are widely applied in the catalytic oxidation of various organic pollutants and the selective reduction of NO (SCR) due to the excellent ability of Ag species for adsorption and dissociation of oxygen. However, the specific effect of the physical-chemical states of Ag species on the catalytic performance for DMF oxidation was rarely studied. As reported previously, oxygen vacancies are helpful to anchoring of noble metal species [31,32], which is highly related to the exposed facets of CeO_2 supports. Accordingly, the contents of surface oxygen vacancies were carefully measured by Raman, EPR and XPS. For three morphology-controlled CeO_2 supports, r-Ce support possessed the maximum content of surface oxygen vacancies, c-Ce support followed and o-Ce support was the lowest, which was consistent with the formation energy of oxygen vacancies for each crystal facets. Abundant surface oxygen vacancies on r-Ce support more contributed to the highly dispersed Ag species than other two CeO_2 supports, as confirmed by XRD and EDS-Mapping results. Besides, the metal-support interaction (MSI) between CeO_2 supports and Ag species was also influenced by the exposed facets, which was enhanced by the charge transfer between Ce^{3+} and Ag^+ . The MSI between Ag species and r-Ce support should be



Scheme 1. Distribution and chemical states of Ag species on CeO_2 supports with different exposed crystal facets.

much stronger due to the high content of Ce^{3+} on (110) and (100) facets, which also hindered the mobility and aggregation of Ag species during the calcination process, while MSI was the weakest for o-Ce support due to deficient of Ce^{3+} on (111) facet. The content of Ce^{3+} was positively related with the content of Ag^+ by controlling the interaction between CeO_2 support and Ag species (Fig. S10). Additionally, the valence state of Ag species was subject to MSI, generally, Ag_2O decomposed easily into Ag and O_2 at relatively low temperature about 300 °C especially on supports with the weak MSI [33]. Thus, metallic Ag^0 species on Ag/o-Ce catalyst was dominated because of the weak interaction between Ag and (111) facets while more Ag^+ species was detected over Ag/r-Ce catalyst. Therefore oxygen vacancy and Ce^{3+} determined the particle sizes and chemical state of Ag species by anchoring of Ag species and MSI between CeO_2 supports and Ag species (Scheme 1).

As shown in Fig. 9A, T_{90} for the catalytic oxidation of DMF were obtained at 158 °C, 223 °C and 296 °C on Ag/r-Ce, Ag/c-Ce and Ag/o-Ce catalysts and reduced by 82 °C, 62 °C and 32 °C compared with the corresponding CeO_2 supports (T_{90} were 240 °C, 285 °C and 328 °C for r-

Ce, c-Ce and o-Ce supports). This indicated that the exposed crystal facet of CeO_2 supports played a decisive role on the catalytic activity, more importantly, the enhanced activity owing to incorporation of Ag species was also dependent on the exposed crystal facet. Fig. 9B further showed the relevancy between T_{90} of DMF or NO yield (as an index product for evaluating the oxidation ability of catalysts) and the content of Ag^+ species, in which Ag^+ showed a negative relationship with T_{90} , but a positive relationship with NO yield (at the complete oxidation temperature, 240 °C). For the catalytic oxidation of DMF, understanding and inhibiting the formation of DMA and NO as byproducts were very critical, for example, the generation of NO was highly related to the excessive oxidation of N element but the formed NO could be eliminated through a SCR process (Ag-based catalyst was widely regarded as a good candidate for SCR [6,7]), which was controlled by reaction temperature, the state of oxygen and Ag species. Therefore, Ag/r-Ce catalysts with 2.5 and 10 wt.% Ag were prepared to adjust the content of Ag^+ and evaluated for the catalytic oxidation of DMF to further confirm the role of Ag^+ species. A lower NO yield was detected on 2.5 wt.% Ag/r-Ce catalyst at the complete oxidation temperature (240 °C) but increased stepwise with increasing the reaction temperature (similar to pristine CeO_2 , Fig. S11), while 5 wt.% and 10 wt.% Ag/r-Ce catalysts presented a decreasing NO yield in a wide temperature range (from 240 °C to 330 °C) and then increased (Fig. 9C). As shown in XPS results (Fig. S12), the different contents of Ag^+ species could be obtained through variation of Ag loading, 80% (2.0 wt.%), 49% (2.45 wt.%) and 20% (2.0 wt.%) Ag^+ was determined on 2.5 wt.%, 5 wt.% and 10 wt.% Ag/r-Ce catalysts, respectively. Thus, it can be inferred that Ag^+ is mainly responsible for formation of NO, while presence of Ag^0 species is conducive to elimination of NO due to SCR effect. Certainly, the roles of oxygen species (they represent the redox ability and depend on surface oxygen vacancies and Ag-O-Ce interfaces) are considerable for DMF

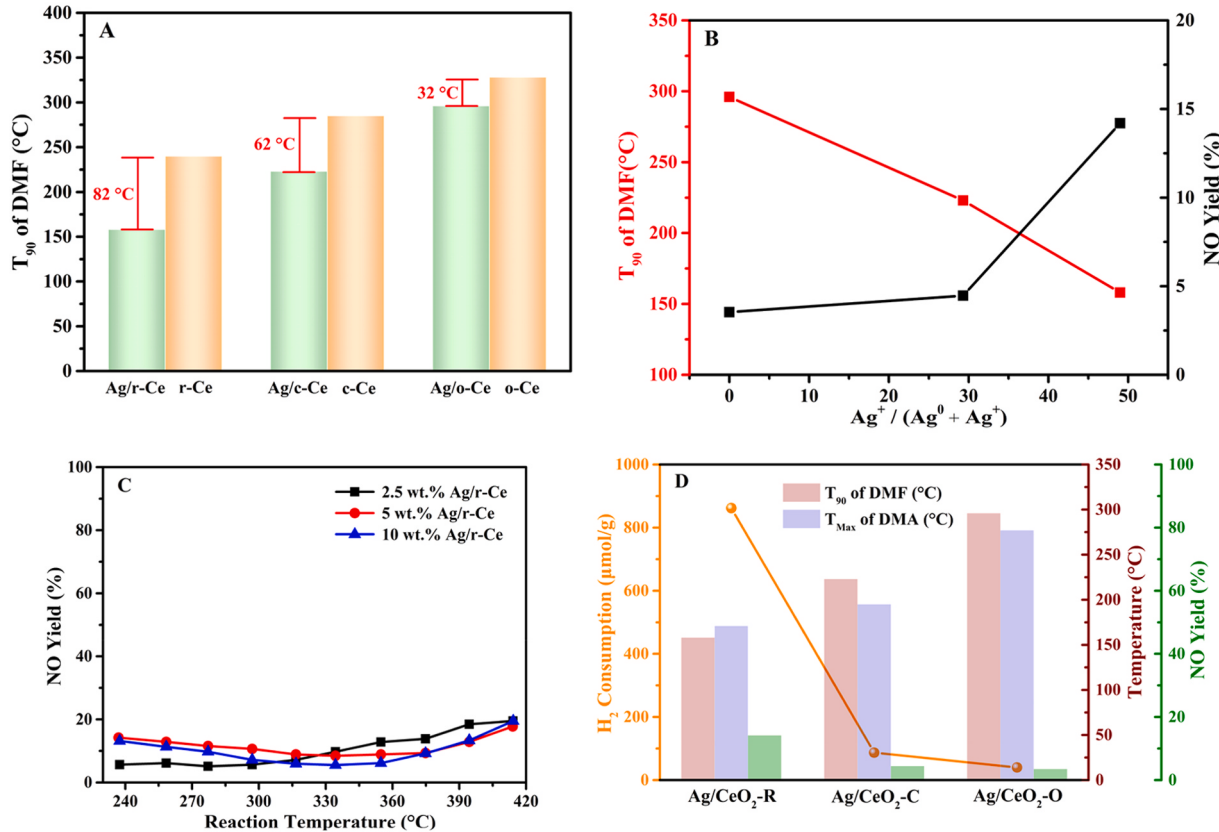


Fig. 9. Comparison of T_{90} of DMF oxidation over CeO_2 and Ag/CeO_2 catalysts (A) and the relationship between Ag^+ content and T_{90} of DMF or NO yield at complete oxidation temperature (B). NO yield of Ag/CeO_2 catalysts with different Ag loadings (C). The relationship between H_2 consumption and T_{90} of DMF oxidation, peak temperature of DMA concentration and NO yield at complete oxidation temperature (D).

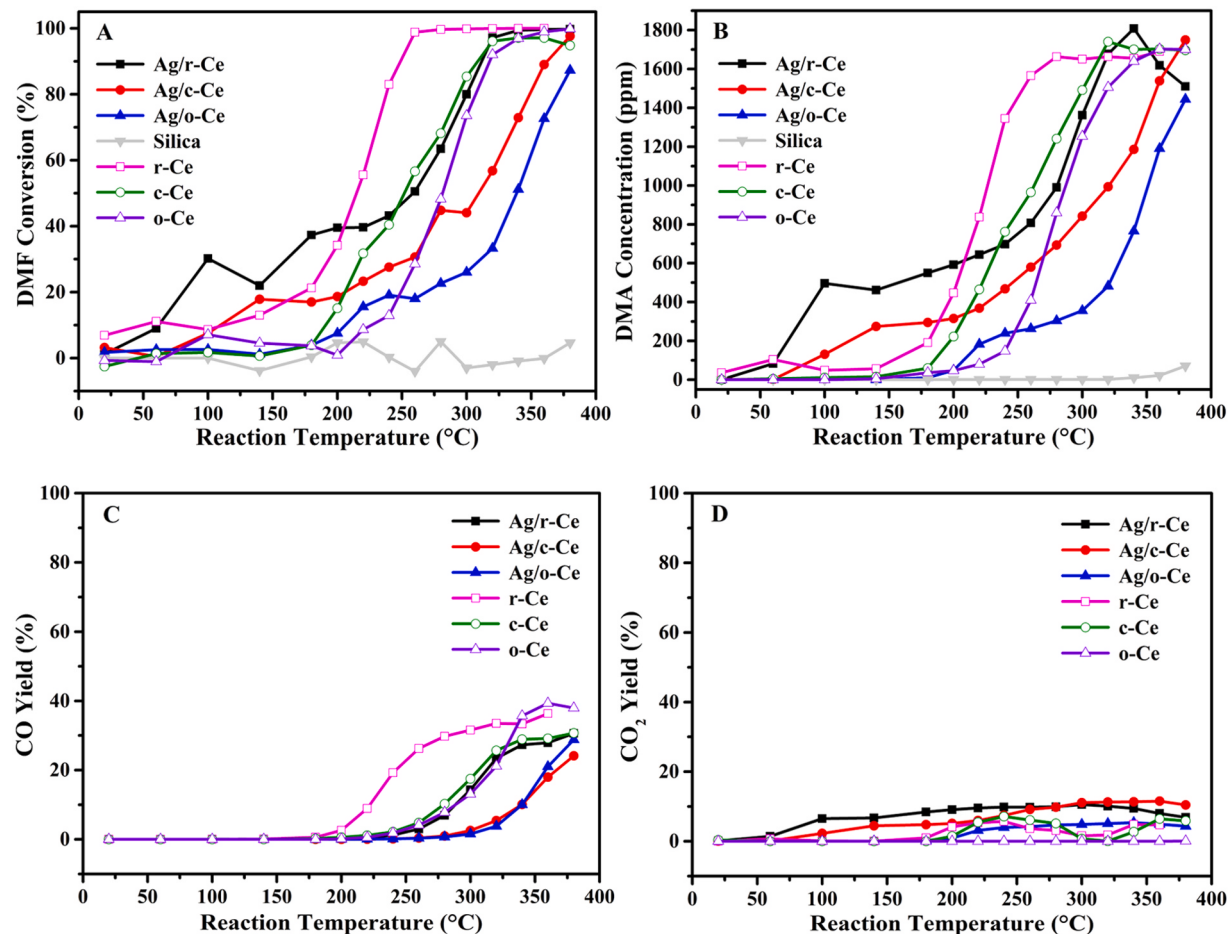


Fig. 10. Catalytic activity of CeO₂ and Ag/CeO₂ catalysts for DMF decomposition under oxygen-free atmosphere (A), the concentration of DMA (B), and the yields of CO (C) and CO₂ (D).

oxidation such as catalytic activity, formation of DMA and NO yield. Fig. 9D displayed the dependency relationship between H₂ consumption and T₉₀ of DMF oxidation, the peak temperature of DMA concentration and NO yield at the temperature of all organic compounds' complete oxidation. Obviously, more active oxygen species contribute to oxidation of DMF and DMA, but also lead to formation of more NO, thus, the redox ability for an optimized catalyst should be emphasized.

The decomposition of DMF under oxygen-free atmosphere was conducted and showed in Fig. 10A, DMF could be completely decomposed under oxygen-free atmosphere but the major products were DMA, CO₂, CO and H₂O. T₉₀ of DMF conversion was as follow: r-Ce (249 °C) < c-Ce (308 °C) < Ag/r-Ce (313 °C) < o-Ce (325 °C) < Ag/c-Ce (364 °C) < Ag/o-Ce (380 °C) while loading of Ag suppressed DMF decomposition, however, the decomposition of DMF could not occur over silica. This result revealed that decomposition of DMF mainly occurred on the oxygen vacancy, and was confirmed by the ratios of O_V / (O_V + O_L) calculated by XPS (Table 1) with the order of r-Ce (26.0%) > c-Ce (23.8%) > o-Ce (21.7%) and Ag/r-Ce (25.2%) > Ag/c-Ce (23.2%) > Ag/o-Ce (20.6%). The surface adsorbed oxygen and lattice oxygen species were in charge of deep oxidation of DMA and CO. Fig. 10B, C and D revealed that introduction of Ag promoted generation of CO₂ and even 100% CO₂ yield was obtained in low temperature range over Ag/r-Ce and Ag/c-Ce catalysts, which was consistent with abundant adsorbed oxygen species and excellent mobility of lattice oxygen on Ag/r-Ce and Ag/c-Ce catalysts from the characterization results mentioned above. Therefore the lattice oxygen species were directly involved in the oxidation of DMF.

3.3.2. *In situ* DRIFTS of DMF oxidation mechanism

In situ DRIFTS was carried out to study the adsorption and oxidation of DMF on pristine r-Ce and Ag/r-Ce catalysts and presented in Fig. 11. Under oxygen-free atmosphere, a series of bands at 1650 cm⁻¹ (C=O stretching of DMF), 1590 cm⁻¹ and 1365 cm⁻¹ (OOCN moiety in OOCN (CH₃)₂, the dehydrogenation of dissociated DMF) [34], 1565 cm⁻¹ (N-H bending of DMA), 1380 cm⁻¹ (deformation vibration of NCH or anti-symmetric deformation vibration of CH₃), 1265 cm⁻¹ (C-N stretching), 1105 cm⁻¹ and 1030 cm⁻¹ (in-plane vibration of CH₃), were observed for adsorption of DMF on pristine r-Ce catalyst (Fig. 11A), which was assigned to the typical characteristic bands of DMA and DMF and also revealed that dissociation of DMF occurred. With increasing reaction temperature, the conversion of DMF into DMA was clearly visible based on the intensity change of bands at 1650 cm⁻¹ (DMF) and 1590/1565 cm⁻¹ (dissociated DMF and DMA), more importantly, new bands ascribed to carboxylate species such as 1540 cm⁻¹ and 1350 cm⁻¹ (vibration of absorbed carboxylate groups) appeared above 200 °C, which indicated that dissociation of DMF and formation/oxidation of DMA occurred and the surface lattice oxygen of CeO₂ was involved directly. Additionally, DRIFTS of DMA adsorption was conducted and the product distribution of DMA oxidation was also analyzed by GC-MS (Figs. S13 and S14), which further confirmed that DMA was the main organic product during decomposition of DMF and the further elimination of DMA through the dehydrogenation of methyl and generation of new amide. After introduction of Ag, the bands assigned to DMA and DMF were detected and similar to the pristine CeO₂, however, the intensity of band at 1650 cm⁻¹ rapidly decreased and even almost disappeared above 250 °C while that at 1590/1565 cm⁻¹ continuously

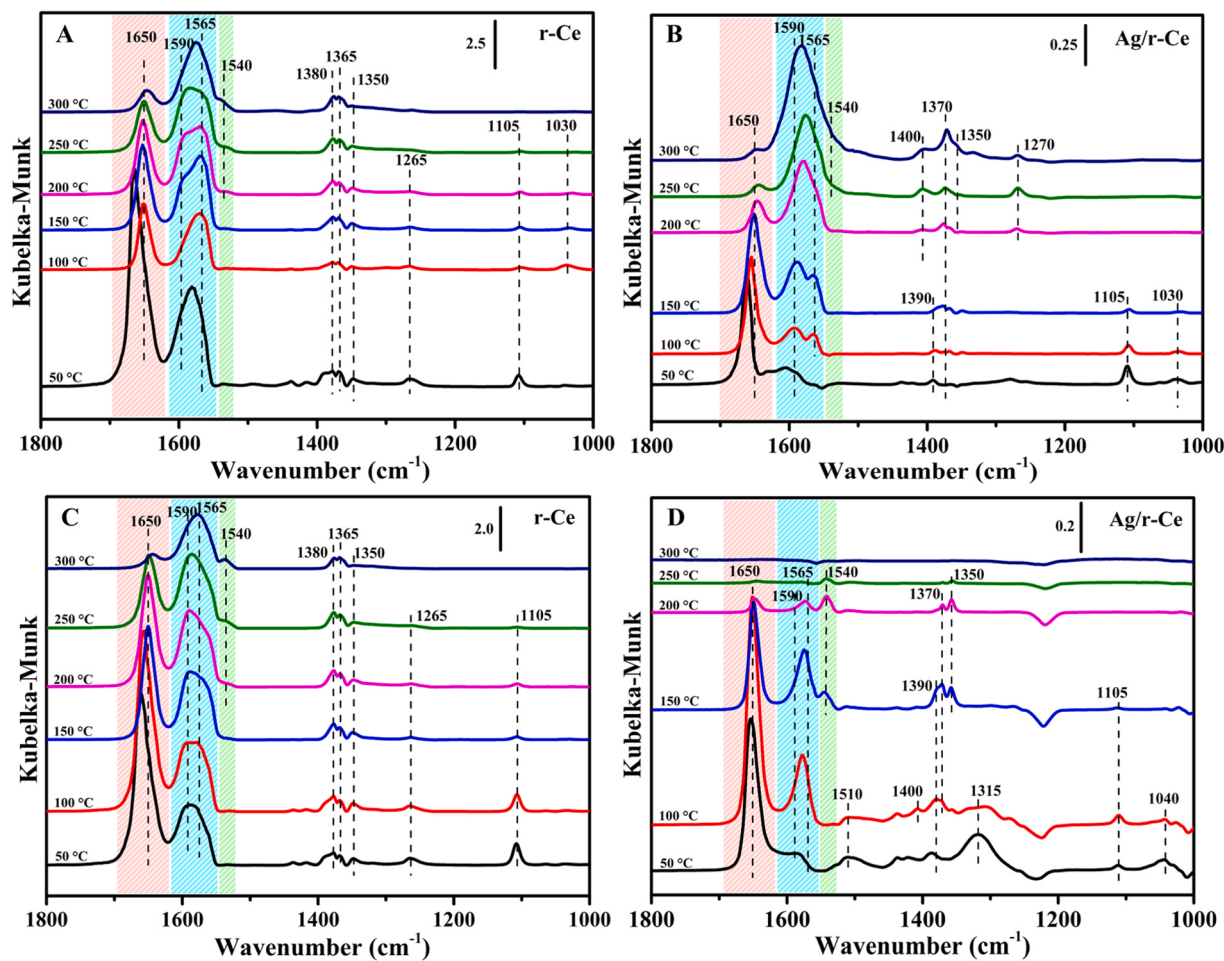
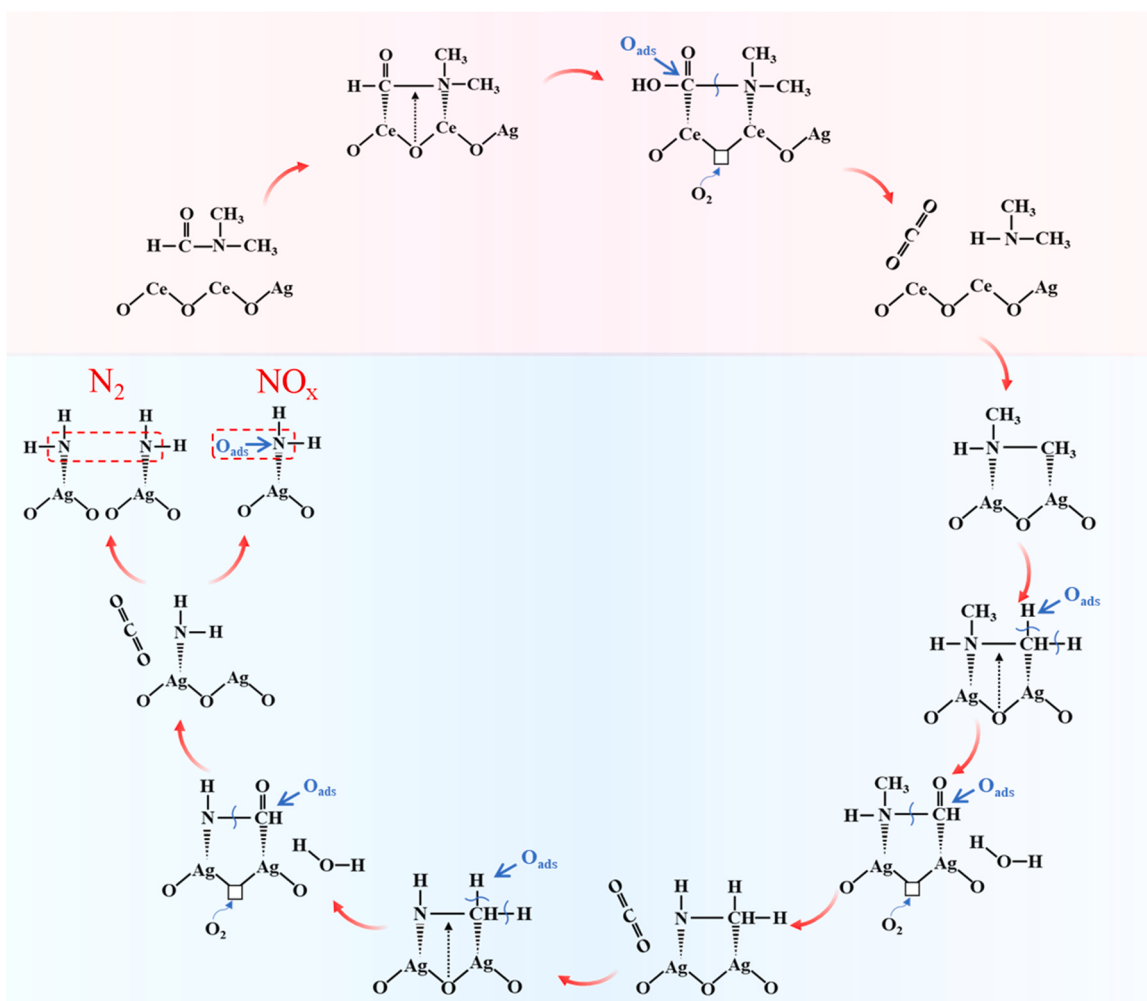


Fig. 11. In situ DRIFTS of DMF adsorption on r-Ce (A) and Ag/r-Ce (B) catalyst and oxidation on r-Ce (C) and Ag/r-Ce (D) catalysts.

increased. After gaseous oxygen was introduced, the infrared characteristic bands on the pristine r-Ce were coincident with those of gaseous oxygen-free, but the band (1540 cm^{-1}) assigning to carboxylate species was more visible because of easily replenishing of surface lattice oxygen of ceria through the gaseous oxygen. Unfortunately, this band still did not disappear even at $300\text{ }^\circ\text{C}$, its deep oxidation was difficult only through the surface lattice oxygen or surface adsorbed oxygen of CeO_2 . The change of characteristic bands on Ag/r-Ce catalyst further suggested that dissociation of DMF and its deep oxidation were obviously enhanced by loading of Ag, for example, the generation of carboxylate species as the intermediate of DMF oxidation could occur at lower temperature compared with the pristine CeO_2 and that of gaseous oxygen-free, which was associated with the enhanced migration ability of lattice oxygen due to Ag-O-Ce interface. More importantly, these carboxylate species and the dissociated DMA completely disappeared above $250\text{ }^\circ\text{C}$ and the complete oxidation of DMF occurred, which further indicated that Ag species enhanced the oxidizing ability of CeO_2 (including the migration of lattice oxygen and the activity of adsorbed oxygen). Figs. S15 and S16 also displayed DRIFTS of DMF adsorption or oxidation over the pristine c-Ce and o-Ce samples and their corresponding Ag supported catalysts without/with gaseous O_2 , similar bands to the pristine r-Ce and Ag/r-Ce catalyst were observed with only a slight difference in the intensity and the reaction temperature, which indicated that the possible dissociation and oxidation mechanisms of DMF were basically identical to Ag/r-Ce catalyst but different in catalytic activity due to difference in oxygen vacancies, mobility of lattice oxygen and Ag-O-Ce interface (replenishing lattice oxygen).

According to tailoring of Ag species via different CeO_2 exposed

crystal facets, the discussion of structure-activity relationship and in situ DRIFTS, a stepwise reaction mechanism for the catalytic oxidation of DMF on Ag/ CeO_2 catalyst is proposed in Scheme 2: dissociation of C(O)-N bond of DMF and further oxidation of the generated DMA. Firstly, DMF is adsorbed on active sites such as oxygen vacancies, $\text{Ce}^{3+}/\text{Ce}^{4+}$ or Ag^+ species via N and C element in DMF, meanwhile dissociation of C(O)-N bond occurs (which can be facilitated through the hydrolysis process in presence of H_2O) and DMF is directly ruptured to the adsorption-activated -CHO and - $\text{N}(\text{CH}_3)_2$ species. Moreover, H-C(O)N(CH_3)₂ bond can also be activated due to presence of Ag^0 species and the activated hydrogen combines with - $\text{N}(\text{CH}_3)_2$ to form DMA, incidentally Ag^0 species also promote reduction of the overoxidized product NO_x into N_2 through a SCR route owing to the activation of C-H bonds in the course of the subsequent reaction. Then the surface-active oxygen species in oxygen vacancies (O_{ads}) or Ag-O-Ce interfaces easily oxidize the activated -CHO into H_2O and CO_x , while the formed DMA is re-adsorbed and activated. Sequentially, the activation of C-H bonds (on Ag^0 species) and the dehydrogenation-oxidation into H_2O (by O_{ads}), the insertion oxidation of surface lattice oxygen ($\text{O}_{\text{latt-surface}}$) forming -HCO and the deep oxidation into H_2O and CO_x stepwise and repeatedly occur, meanwhile the depleted surface lattice oxygen can be quickly replenished by gaseous O_2 and Ag-O-Ce interfaces. After the stepwise oxidation of - CH_3 is finished, the two adjacent adsorbed - NH_2 species combine into the final inorganic product N_2 , but the surface adsorbed oxygen species can also interact with the - NH_2 directly to form the undesirable NO or even NO_2 byproducts.



Scheme 2. Proposed mechanism of DMF oxidation on Ag/r-Ce catalyst.

4. Conclusions

In this work, Ag/CeO₂ catalysts were prepared by a simple incipient wetness impregnation method using cerium oxide with different exposed crystal facets such as nanorods (110) and (100), nanocubes (100) and nano-octahedrons (111) as support, and then the catalytic oxidation of DMF as a representative NVOCs was evaluated. Ag/r-Ce catalyst exhibits the best catalytic activity of DMF oxidation ($T_{90} = 158^{\circ}\text{C}$) and about 80% yield of N₂ in the wide range of 237–400 °C, but the complete oxidation temperature is obtained at 240 °C (DMA as the main organic by-product is deeply oxidized into CO_x and N₂/NO_x). Moreover, Ag/r-Ce catalyst exhibits an unexceptionable H₂O-resistance (with an enhanced activity), high stability at 240 °C (at least 120 h) and only a slight decline within the initial 20 h even at 170 °C. The catalytic performance of Ag/CeO₂ catalyst for the catalytic oxidation of DMF is closely associated with the exposed crystal facets of CeO₂ support which tailors the physical structure and chemical state of Ag species. More oxygen vacancies on CeO₂ nanorods with (110) and (100) facets lead to the highly dispersed Ag species by the preferential anchoring route and the presence of abundant Ag-O-Ce interfaces (the strong interaction between CeO₂ support and Ag species occurs, attributing to the enhanced mobility of lattice oxygen species and the stabilization of Ag⁺ species). Therefore, the abundant oxygen vacancies, Ag-O-Ce interfaces and the enhanced activity of oxygen species including surface lattice and adsorbed oxygen species are synergistically responsible for the outstanding catalytic performance of Ag/r-Ce catalyst for DMF oxidation. However, the excessive active oxygen species also lead to

generation of the undesirable NO_x whereas Ag/o-Ce catalyst presents a higher N₂ yield, moreover, the presence of metallic Ag⁰ species can reduce the formed NO_x to N₂ through SCR reaction with the organic compounds in the range of 240–320 °C. Based on the complementary experiments and in situ DRIFTS of DMF adsorption and oxidation, a possible mechanism was proposed for the catalytic oxidation of DMF on Ag/CeO₂ catalyst. The dissociation of (O)C-N bond is firstly involved in DMF oxidation, and then the generated -N(CH₃)₂ is stepwise and repeatedly dehydrogenated and partially oxidized via the insertion of surface lattice oxygen, meanwhile the formed -HCO is completely oxidized into CO₂ and H₂O by surface adsorbed oxygen species. Finally, the two adjacent -NH₂ species combine into the final inorganic product N₂. This work contributes to design and preparation of an efficient catalyst for the catalytic oxidation of NVOCs, and provides further insights into the reaction mechanism of DMF oxidation on Ag/CeO₂ catalyst.

CRediT authorship contribution statement

Xiaohan Guo: Conceptualization, Methodology, Data curation, Investigation, Writing – original draft. **Chenxiao Dong:** Methodology, Investigation. **Meixingzi Gao:** Data curation, Investigation. **Dongsheng Ye:** Methodology, Validation. **Qiguang Dai:** Conceptualization, Writing – review & editing. **Wangcheng Zhan:** Validation, Visualization. **Zhiqiang Wang:** DFT data acquisition. **Li Wang:** Formal analysis. **Aiyong Wang:** Supervision, Writing - original draft. **Yun Guo:** Resources, Funding acquisition. **Yanglong Guo:** Supervision, Writing – review &

editing.

Declaration of Competing Interest

The authors declare that they have no known competing financial interests or personal relationships that could have appeared to influence the work reported in this paper.

Data Availability

Data will be made available on request.

Acknowledgements

This work was supported by the National Key Research and Development Program of China (2022YFB3504200), the National Natural Science Foundation of China (U21A20326, 22106101), the fund of the National Engineering Laboratory for Mobile Source Emission Control Technology (NELMS2020A05), and the Fundamental Research Funds for the Central Universities.

Appendix A. Supporting information

Supplementary data associated with this article can be found in the online version at [doi:10.1016/j.apcatb.2023.123286](https://doi.org/10.1016/j.apcatb.2023.123286).

References

- [1] X.X. Duan, T. Zhao, Z.W. Yang, B. Niu, G.G. Li, B.Z. Li, Z.S. Zhang, J. Cheng, Z. P. Hao, Oxygen activation-boosted manganese oxide with unique interface for chlorobenzene oxidation: Unveiling the roles and dynamic variation of active oxygen species in heterogeneous catalytic oxidation process, *Appl. Catal. B: Environ.* 331 (2023), 122719, <https://doi.org/10.1016/j.apcatb.2023.122719>.
- [2] G.T. Chai, W.D. Zhang, L.F. Liotta, M.Q. Li, Y.L. Guo, A. Giroir-Fendler, Total oxidation of propane over Co_3O_4 -based catalysts: Elucidating the influence of Zr dopant, *Appl. Catal. B: Environ.* 298 (2021), 120606, <https://doi.org/10.1016/j.apcatb.2021.120606>.
- [3] R.D. Zhang, P.X. Li, R. Xiao, N. Liu, B.H. Chen, Insight into the mechanism of catalytic combustion of acrylonitrile over Cu-doped perovskites by an experimental and theoretical study, *Appl. Catal. B: Environ.* 196 (2016) 142–154, <https://doi.org/10.1016/j.apcatb.2016.05.025>.
- [4] F. Wang, G.Z. He, B. Zhang, M. Chen, X.Y. Chen, C.B. Zhang, H. He, Insights into the Activation Effect of H_2 Pretreatment on $\text{Ag}/\text{Al}_2\text{O}_3$ Catalyst for the Selective Oxidation of Ammonia, *ACS Catal.* 9 (2019) 1437–1445, <https://doi.org/10.1021/acscatal.8b03744>.
- [5] L. Zhang, H. He, Mechanism of selective catalytic oxidation of ammonia to nitrogen over $\text{Ag}/\text{Al}_2\text{O}_3$, *J. Catal.* 268 (2009) 18–25, <https://doi.org/10.1016/j.jcat.2009.08.011>.
- [6] J. Wang, R. You, K. Qian, Y. Pan, J.Z. Yang, W.X. Huang, Effect of the modification of alumina supports with chloride on the structure and catalytic performance of $\text{Ag}/\text{Al}_2\text{O}_3$ catalysts for the selective catalytic reduction of NO_x with propane and H_2 /propane, *Chin. J. Catal.* 42 (2021) 2242–2253, [https://doi.org/10.1016/S1872-2067\(21\)63904-9](https://doi.org/10.1016/S1872-2067(21)63904-9).
- [7] X.W. Yang, A.Y. Wang, J.F. Guo, Y.L. Guo, Y. Guo, L. Wang, W.C. Zhan, γ - Al_2O_3 supported silver nanoparticle applied in C_3H_8 -SCR: Nanosphere and nanoflake, *Catal. Commun.* 176 (2023), 106634, <https://doi.org/10.1016/j.catcom.2023.106634>.
- [8] J.H. Lee, S.H. Lee, J.W. Choung, C.H. Kim, K.-Y. Lee, Ag-incorporated macroporous CeO_2 catalysts for soot oxidation: Effects of Ag amount on the generation of active oxygen species, *Appl. Catal. B: Environ.* 246 (2019) 356–366, <https://doi.org/10.1016/j.apcatb.2019.01.064>.
- [9] M.V. Grabczenko, G.V. Mamontov, V.I. Zaikovskii, V. La Parola, L.F. Liotta, O. V. Vodyankina, The role of metal-support interaction in Ag/CeO_2 catalysts for CO and soot oxidation, *Appl. Catal. B: Environ.* 260 (2020), 118148, <https://doi.org/10.1016/j.apcatb.2019.118148>.
- [10] H.L. Wang, S.T. Luo, M.S. Zhang, W. Liu, X.D. Wu, S. Liu, Roles of oxygen vacancy and O_x in oxidation reactions over CeO_2 and Ag/CeO_2 nanorod model catalysts, *J. Catal.* 368 (2018) 365–378, <https://doi.org/10.1016/j.jcat.2018.10.018>.
- [11] L. Ma, D.S. Wang, J.H. Li, B.Y. Bai, L.X. Fu, Y.D. Li, Ag/CeO_2 nanospheres: Efficient catalysts for formaldehyde oxidation, *Appl. Catal. B: Environ.* 148–149 (2014) 36–43, <https://doi.org/10.1016/j.apcatb.2013.10.039>.
- [12] C.-C. Ou, C.-H. Chen, T.-S. Chan, C.-S. Chen, S. Cheng, Influence of pretreatment on the catalytic performance of Ag/CeO_2 for formaldehyde removal at low temperature, *J. Catal.* 380 (2019) 43–54, <https://doi.org/10.1016/j.jcat.2019.09.028>.
- [13] M.H. Liu, X.D. Wu, S. Liu, Y.X. Gao, Z. Chen, Y. Ma, R. Ran, D. Weng, Study of Ag/CeO_2 catalysts for naphthalene oxidation: Balancing the oxygen availability and oxygen regeneration capacity, *Appl. Catal. B: Environ.* 219 (2017) 231–240, <https://doi.org/10.1016/j.apcatb.2017.07.058>.
- [14] T. Nanba, S. Masukawa, J. Uchisawa, A. Obuchi, Effect of support materials on Ag catalysts used for acrylonitrile decomposition, *J. Catal.* 259 (2008) 250–259, <https://doi.org/10.1016/j.jcat.2008.08.013>.
- [15] E. Aneggi, J. Llorca, C. de Leitenburg, G. Dolcetti, A. Trovarelli, Soot combustion over silver-supported catalysts, *Appl. Catal. B: Environ.* 91 (2009) 489–498, <https://doi.org/10.1016/j.apcatb.2009.06.019>.
- [16] H. Zhang, X.H. Gao, B.W. Gong, S.J. Shao, C.S. Tu, J. Pan, Y.Y. Wang, Q.G. Dai, Y. L. Guo, X.Y. Wang, Catalytic combustion of CVOCs over $\text{MoO}_x/\text{CeO}_2$ catalysts, *Appl. Catal. B: Environ.* 310 (2022), 121240, <https://doi.org/10.1016/j.apcatb.2022.121240>.
- [17] M. Nolan, S.C. Parker, G.W. Watson, The electronic structure of oxygen vacancy defects at the low index surfaces of ceria, *Surf. Sci.* 595 (2005) 223–232, <https://doi.org/10.1016/j.susc.2005.08.015>.
- [18] Q.G. Dai, H. Huang, Y. Zhu, W. Deng, S.X. Bai, X.Y. Wang, G.Z. Lu, Catalysis oxidation of 1,2-dichloroethane and ethyl acetate over ceria nanocrystals with well-defined crystal planes, *Appl. Catal. B: Environ.* 117–118 (2012) 360–368, <https://doi.org/10.1016/j.apcatb.2012.02.001>.
- [19] C.W. Li, Y. Sun, I. Djerdj, P. Voepel, C.-C. Sack, T. Weller, R. Ellinghaus, J. Sann, Y. L. Guo, B.M. Smarsly, H. Over, Shape-Controlled CeO_2 Nanoparticles: Stability and Activity in the Catalyzed HCl Oxidation Reaction, *ACS Catal.* 7 (2017) 6453–6463, <https://doi.org/10.1021/acscatal.7b01618>.
- [20] H. Huang, Q.G. Dai, X.Y. Wang, Morphology effect of Ru/CeO_2 catalysts for the catalytic combustion of chlorobenzene, *Appl. Catal. B: Environ.* 158–159 (2014) 96–105, <https://doi.org/10.1016/j.apcatb.2014.01.062>.
- [21] Z. Wang, Z.P. Huang, J.T. Brosnahan, S. Zhang, Y.L. Guo, Y. Guo, L. Wang, Y. S. Wang, W.C. Zhan, Ru/ CeO_2 Catalyst with Optimized CeO_2 Support Morphology and Surface Facets for Propane Combustion, *Environ. Sci. Technol.* 53 (2019) 5349–5358, <https://doi.org/10.1021/acs.est.9b01929>.
- [22] H.C. Sun, H. Wang, Z.P. Qu, Construction of CuO/CeO_2 Catalysts via the Ceria Shape Effect for Selective Catalytic Oxidation of Ammonia, *ACS Catal.* 13 (2023) 1077–1088, <https://doi.org/10.1021/acscatal.2c05168>.
- [23] S.J. Chang, M. Li, Q. Hua, L.J. Zhang, Y.S. Ma, B.J. Ye, W.X. Huang, Shape-dependent interplay between oxygen vacancies and Ag/CeO_2 interaction in Ag/CeO_2 catalysts and their influence on the catalytic activity, *J. Catal.* 293 (2012) 195–204, <https://doi.org/10.1016/j.jcat.2012.06.025>.
- [24] W. Wang, Y.J. Liu, L. Wang, W.C. Zhan, Y.L. Guo, Y. Guo, Soot combustion over Ag catalysts supported on shape-controlled CeO_2 , *Catal. Today* 376 (2021) 9–18, <https://doi.org/10.1016/j.cattod.2020.10.043>.
- [25] F.Y. Huang, D.S. Ye, X.H. Guo, W.C. Zhan, Y. Guo, L. Wang, Y.S. Wang, Y.L. Guo, Effect of ceria morphology on the performance of $\text{MnO}_x/\text{CeO}_2$ catalysts in catalytic combustion of N, N-dimethylformamide, *Catal. Sci. Technol.* 10 (2020) 2473–2483, <https://doi.org/10.1039/C9CY02384D>.
- [26] Y. Zhang, J.C. Lu, L.M. Zhang, T. Fu, J. Zhang, X. Zhu, X.Y. Gao, D.D. He, Y.M. Luo, D.D. Dionysiou, W.J. Zhu, Investigation into the catalytic roles of oxygen vacancies during gaseous styrene degradation process via CeO_2 catalysts with four different morphologies, *Appl. Catal. B: Environ.* 309 (2022), 121249, <https://doi.org/10.1016/j.apcatb.2022.121249>.
- [27] M.Y. Cui, J.X. He, N.P. Lu, Y.Y. Zheng, W.J. Dong, W.H. Tang, B.Y. Chen, C.R. Li, Morphology and size control of cerium carbonate hydroxide and ceria micro/nanostructures by hydrothermal technology, *Mater. Chem. Phys.* 121 (2010) 314–319, <https://doi.org/10.1016/j.matchemphys.2010.01.041>.
- [28] Z. Hu, X.F. Liu, D.M. Meng, Y. Guo, Y.L. Guo, G.Z. Lu, Effect of Ceria Crystal Plane on the Physicochemical and Catalytic Properties of Pd/Ceria for CO and Propane Oxidation, *Accts Catal.* 6 (2016) 2265–2279, <https://doi.org/10.1021/acscatal.5b02617>.
- [29] J.J. Kong, Z.W. Xiang, G.Y. Li, T.C. An, Introduce oxygen vacancies into CeO_2 catalyst for enhanced coke resistance during photothermocatalytic oxidation of typical VOCs, *Appl. Catal. B: Environ.* 269 (2020), 118755, <https://doi.org/10.1016/j.apcatb.2020.118755>.
- [30] A.A. Marciniak, O.C. Alves, L.G. Appel, C.J.A. Mota, Synthesis of dimethyl carbonate from CO_2 and methanol over CeO_2 : Role of copper as dopant and the use of methyl trichloroacetate as dehydrating agent, *J. Catal.* 371 (2019) 88–95, <https://doi.org/10.1016/j.jcat.2019.01.035>.
- [31] X.-Q. Gong, A. Selloni, O. Dulub, P. Jacobson, U. Diebold, Small Au and Pt Clusters at the Anatase TiO_2 (101) Surface: Behavior at Terraces, Steps, and Surface Oxygen Vacancies, *J. Am. Chem. Soc.* 130 (2008) 370–381, <https://doi.org/10.1021/ja0773148>.
- [32] Y.K. Zhang, Y.H. Wang, K.B. Su, F.P. Wang, The influence of the oxygen vacancies on the Pt/ TiO_2 single-atom catalyst—a DFT study, *J. Mol. Model.* 28 (2022) 175, <https://doi.org/10.1007/s00894-022-05123-w>.
- [33] K.-i Shimizu, H. Kawachi, A. Satsuma, Study of active sites and mechanism for soot oxidation by silver-loaded ceria catalyst, *Appl. Catal. B: Environ.* 96 (2010) 169–175, <https://doi.org/10.1016/j.apcatb.2010.02.016>.
- [34] J.-L. Lin, Y.-C. Lin, B.-C. Lin, P.-C. Lai, T.-E. Chien, S.-H. Li, Y.-F. Lin, Adsorption and Reactions on TiO_2 : Comparison of N, N-Dimethylformamide and Dimethylamine, *J. Phys. Chem. C* 118 (2014) 20291–20297, <https://doi.org/10.1021/jp5044859>.